OMC-2 FIR 4 under the microscope: Shocks, filaments, and a highly collimated jet at 100 au scales

L. Chahine, A. López-Sepulcre, L. Podio, C. Codella, R. Neri, S. Mercimek, M. de Simone, P. Caselli, C. Ceccarelli, M. Bouvier, et al.

▶ **To cite this version:**

L. Chahine, A. López-Sepulcre, L. Podio, C. Codella, R. Neri, et al.. OMC-2 FIR 4 under the microscope: Shocks, filaments, and a highly collimated jet at 100 au scales. Astronomy and Astrophysics - A&A, 2022, 667, 10.1051/0004-6361/202243799 . insu-03860269

HAL Id: insu-03860269

https://insu.hal.science/insu-03860269

Submitted on 19 Nov 2022

HAL is a multi-disciplinary open access archive for the deposit and dissemination of scientific research documents, whether they are published or not. The documents may come from teaching and research institutions in France or abroad, or from public or private research centers.

L'archive ouverte pluridisciplinaire **HAL**, est destinée au dépôt et à la diffusion de documents scientifiques de niveau recherche, publiés ou non, émanant des établissements d'enseignement et de recherche français ou étrangers, des laboratoires publics ou privés.

Distributed under a Creative Commons Attribution 4.0 International License

A&A 667, A6 (2022)
https://doi.org/10.1051/0004-6361/202243799
© L. Chahine et al. 2022

Astronomy & Astrophysics

OMC-2 FIR 4 under the microscope: Shocks, filaments, and a highly collimated jet at 100 au scales

L. Chahine[1,2], A. López-Sepulcre[1,3], L. Podio[4], C. Codella[4,3], R. Neri[1], S. Mercimek[4,5], M. De Simone[3,4], P. Caselli[6], C. Ceccarelli[3], M. Bouvier[3], N. Sakai[7], F. Fontani[3], S. Yamamoto[8], F. O. Alves[6], V. Lattanzi[6], L. Evans[9,4], and C. Favre[3]

[1] Institut de Radioastronomie Millimétrique (IRAM), 300 rue de la Piscine, 38406 Saint-Martin-d'Hères, France
e-mail: chahine@iram.fr
[2] Université Grenoble Alpes, 38000 Grenoble, France
[3] Université Grenoble Alpes, CNRS, IPAG, 38000 Grenoble, France
[4] INAF, Osservatorio Astrofisico di Arcetri, Largo E. Fermi 5, 50125, Firenze, Italy
[5] Università degli Studi di Firenze, Dipartimento di Fisica e Astronomia, Via G. Sansone 1, 50019 Sesto Fiorentino, Italy
[6] Center for Astrochemical Studies, Max Planck Institute for Extraterrestrial Physics, Garching 85748, Germany
[7] The Institute of Physical and Chemical Research (RIKEN), Saitama 351-0198, Japan
[8] Department of Physics, The University of Tokyo, Bunkyo-ku, Tokyo 113-0033, Japan
[9] IRAP, Université de Toulouse, 9 avenue du colonel Roche, 31028 Toulouse Cedex 4, France

Received 15 April 2022 / Accepted 1 September 2022

ABSTRACT

Context. Star-forming molecular clouds are characterised by the ubiquity of intertwined filaments. The filaments have been observed in both high- and low-mass star-forming regions, and they are thought to split into collections of sonic fibres. The locations where filaments converge are termed hubs, and these are associated with the young stellar clusters. However, the observations of filamentary structures within hubs at distances of 75–300 pc require a high angular resolution <2″ (~150–600 au) that limits the number of such studies conducted so far.

Aims. The integral shaped filament (ISF) of the Orion A molecular cloud is noted for harbouring several hubs within which no filamentary structures have been observed so far. The goal of our study is to investigate the nature of the filamentary structures within one of these hubs, which is the chemically rich hub OMC-2 FIR 4, and to analyse their emission with high density and shock tracers.

Methods. We observed the OMC-2 FIR 4 proto-cluster using Band 6 of the Atacama Large (sub-)Millimetre Array (ALMA) in Cycle 4 with an angular resolution of ~0.26″ (100 au). We analysed the spatial distribution of dust, the shock tracer SiO, and dense gas tracers (i.e., CH_3OH, CS, and $H^{13}CN$). We also studied the gas kinematics using SiO and CH_3OH maps.

Results. Our observations for the first time reveal interwoven filamentary structures within OMC-2 FIR 4 that are probed by several tracers. Each filamentary structure is characterised by a distinct velocity as seen from the emission peak of CH_3OH lines. They also show transonic and supersonic motions. SiO is associated with filaments and also with multiple bow-shock features. The bow-shock features have sizes between ~500 and 2700 au and are likely produced by the outflow from HOPS-370. Their dynamical ages are <800 yr. In addition, for the first time, we reveal a highly collimated SiO jet (~1°) with a projected length of ~5200 au from the embedded protostar VLA15.

Conclusions. Our study unveiled the previously unresolved filamentary structures as well as the shocks within OMC-2 FIR 4. The kinematics of the filamentary structures might be altered by external and/or internal mechanisms such as the wind from H II regions, the precessing jet from the protostellar source HOPS-370, or the jet from VLA 15. While the complexity of the region, coupled with the limited number of molecular lines in our dataset, makes any clear association with these mechanisms challenging, our study shows that multi-scale observations of these regions are crucial for understanding the accretion processes and flow of material that shape star formation.

Key words. stars: formation – methods: observational – ISM: molecules – ISM: kinematics and dynamics – ISM: jets and outflows – ISM: individual objects: OMC-2 FIR 4

1. Introduction

The interstellar medium (ISM) is highly filamentary on all scales. Networks of intricate filaments are seen in low- and high-mass star-forming regions, and even in clouds where no star formation is yet ongoing (e.g. Goldsmith et al. 2008; André et al. 2014; Molinari et al. 2014; Orkisz et al. 2019; Chung et al. 2021). In recent years, high angular resolution studies have shown that the filaments split into small-scale and velocity-coherent elongated structures, called fibres, which in turn fragment into the dense cores we observe today (e.g. Hacar et al. 2013, 2017b; Tafalla & Hacar 2015; Henshaw et al. 2017; Sokolov et al. 2019). Among star-forming regions, the Orion A cloud is noted for its prominent filamentary structures in both CO and dust maps (e.g. Bally et al. 1987; Chini et al. 1997; Johnstone & Bally 1999; Shimajiri et al. 2011; Polychroni et al. 2013; André et al. 2014; Suri et al. 2019). Within this cloud lies the well-known integral shaped filament (ISF; Bally et al. 1987), the most massive

Open Access article, published by EDP Sciences, under the terms of the Creative Commons Attribution License (https://creativecommons.org/licenses/by/4.0), which permits unrestricted use, distribution, and reproduction in any medium, provided the original work is properly cited.
This article is published in open access under the Subscribe-to-Open model. Subscribe to A&A to support open access publication.

filament in the solar neighbourhood with a total mass per unit length ($M_{\rm lin} \sim 500\,M_\odot\,{\rm pc}^{-1}$; Bally et al. 1987). The ISF is located at a distance of ~393±25 pc (Grossschedl et al. 2018). Several studies have found that the ISF consists of substructures of small-scale (<1 pc) sub-filaments or fibres (e.g. Martin-Pintado et al. 1990; Rodriguez-Franco et al. 1992; Shimajiri et al. 2011; Li et al. 2013; Hacar et al. 2017a, 2018; Zhang et al. 2020) and condensations or hub-filament structures (hubs) (Mezger et al. 1990; Chini et al. 1997; Myers 2009; Shimajiri et al. 2011; Hacar et al. 2018). In turn, the latter are thought to contain complex nets of fibres (Hacar et al. 2018) or of filamentary structures. However, the filamentary structures within the hubs along the ISF were not resolved at 4.″5 resolution (~2000 au; Hacar et al. 2018). To our knowledge, filamentary structures within a hub were only observed within IRAS4A at 300 pc. They have sizes ≤450 au (De Simone et al. 2022). To observe similar structures within the hubs of the ISF, an angular resolution of about 2″ or smaller (<600 au) is therefore required. Because the filament and fibre nomenclature refers to structures at larger scales, we decided to adopt the name "filamentary structures" for those at <1000 au scales.

In this work, we focus on the intermediate-mass hub OMC-2 FIR 4, an archetypical Sun-like star-forming region along the ISF. This region was identified for the first time as a bright continuum source at 1.3 mm by Mezger et al. (1990). Later, it was observed, studied, and characterised at several wavelengths. Based on its envelope mass and luminosity (~30 $M_\odot$ and ~400 $L_\odot$; Mezger et al. 1990), OMC-2 FIR 4 was considered as an intermediate-mass protostar (Johnstone et al. 2003). However, Shimajiri et al. (2008) discovered that OMC-2 FIR 4 is actually a protostellar cluster hosting several dusty cores and not a single protostar. Since then, OMC-2 FIR 4 was thoroughly studied with different telescopes and at different wavelengths (e.g. Takahashi et al. 2008; Kama et al. 2013, 2015; Furlan et al. 2014; López-Sepulcre et al. 2017; Evans et al. 2022). Its envelope size and luminosity were estimated to be ~10^4 au and ≤1000 $L_\odot$ (Crimier et al. 2009; Furlan et al. 2014). Its systemic velocity is ~11.4 km s^{-1} (Shimajiri et al. 2008; Favre et al. 2018). The clustered nature of OMC-2 FIR 4 was further confirmed by several studies (López-Sepulcre et al. 2013b; Kainulainen et al. 2017; Tobin et al. 2019; Chahine et al. 2022). In addition, more of its physical properties have been revealed. Its outer shell is strongly irradiated by a far-ultraviolet (FUV) field (~1500 G_0, where G_0 is the FUV radiation field in Habing units), arising from the high-mass stars located in the nearby Trapezium OB association (López-Sepulcre et al. 2013a; Favre et al. 2018), and its interior envelope is subject to high irradiation and ionisation by local cosmic ray-like particles with an ionisation rate of $\zeta \sim 4 \times 10^{-14}$ s^{-1} (Ceccarelli et al. 2014; Fontani et al. 2017; Favre et al. 2018). Due to these characteristics, OMC-2 FIR 4 is considered as the nearest analogue of our solar birth environment, which is thought to be a clustered dense environment (Adams 2010; Pfalzner et al. 2015) that was subject to internal irradiation from energetic particles (>10 MeV; Gounelle et al. 2013).

Despite all this progress, several questions still swirl around OMC-2 FIR 4. The observations at parsec and sub-parsec scales using quiescent gas tracers (e.g. N_2H^+; Hacar et al. 2018; Fontani et al. 2020, NH_3; Wu et al. 2018, HC_3N; Tatematsu et al. 2008) have shown that OMC-2 FIR 4 is a hub-filament structure. In this context, the open questions are whether filamentary structures exist within this hub, and if they might be observed at protocluster scale (≤0.1 pc) using dynamic gas tracers (such as SiO and CH_3OH), as in the case of NGC 1333 IRAS 4A (De Simone et al. 2022). The differences that might arise from this type of observations compared to the studies performed at large scales are unclear. The same applies to the differences between the dynamic gas (traced by, e.g., SiO and CH_3OH) and the quiescent gas (traced by, e.g., N_2H^+ and NH_3). Another important question we also address is the presence of jets and outflows. It is known that within the protocluster, the hot corino HOPS-108 drives a jet towards the south-east (Lattanzi et al. 2021). In addition, OMC-2 FIR 4 is located to the south of the intermediate-mass protostar HOPS-370 that drives an outflow whose southern lobe overlaps, at least in projection, with OMC-2 FIR 4 (Shimajiri et al. 2008). The outflow was detected in several tracers such as CO and [O I] (e.g. Williams et al. 2003; Shimajiri et al. 2008; Takahashi et al. 2008; González-García et al. 2016; Tobin et al. 2019), and several non-thermal jet knots were also discovered (Osorio et al. 2017). However, whether it has triggered the star formation in OMC-2 FIR 4 is still an open question.

Two key molecules that can help to answer these questions and to study the diverse processes that occur in molecular clouds and stellar protoclusters are SiO and CH_3OH. First, SiO is a useful tracer of shocked gas and outflows. During shock processes, gas-grain collisions (sputtering) and grain-grain collisions (shattering) release Si from the grains into the gas phase (Draine et al. 1983; Flower & Pineau des Forets 1994; Schilke et al. 1997; Caselli et al. 1997). Si is oxidised rapidly in SiO, resulting in an increase of SiO abundance in the shocks by several orders of magnitude (Gusdorf et al. 2008a,b; Guillet et al. 2011). On the other hand, CH_3OH is present in different environments such as molecular clouds, photo-dissociation regions (PDR), and hot corinos (e.g. Leurini et al. 2004, 2010; Cuadrado et al. 2017; Maret et al. 2005; Bouvier et al. 2020). It is prevalently formed on dust grains (e.g. Tielens & Hagen 1982; Watanabe & Kouchi 2002; Rimola et al. 2014) and is released into the gas phase via thermal and/or non-thermal processes (e.g. Duley & Williams 1993; Flower & Pineau des Forets 1994; Minissale et al. 2016; Dartois et al. 2019). Hence, CH_3OH can probe different mechanisms that can inject it into the gas phase, such as thermal desorption, shocks, irradiation by UV photons, and cosmic ray bombardment. In this vein, we present the first study of the filamentary structures and shocks within the protostellar cluster OMC-2 FIR 4 at an unprecedented angular resolution of ~100 au, where we targeted eight different molecular tracers, including SiO and CH_3OH, with the Atacama Large (sub-)Millimetre Array (ALMA) at 1.2 mm.

The paper is structured as follows: in Sect. 2 we describe the observations. In Sect. 3, we present the molecular line maps, together with the main results of the analysis. In Sect. 4, we discuss the results, and, finally, in Sect. 5, we summarise the conclusions.

2. Observations

OMC-2 FIR 4 was observed with ALMA during its Cycle 4 operations, between 25 October 2016 and 5 May 2017, as part of the project 2016.1.00376.S (PI: Ana López-Sepulcre). The observations were performed using the ALMA main array in its C-5 configuration, probing angular scales from 0.″19 to 11.″2. Several spectral windows (spw) were placed within the spectral range (218–234 GHz and 243–262 GHz). They were observed using spectral channels of 122.070 kHz (~0.14–0.17 km s^{-1}). A subsequent spectral smoothing by a factor 3 was applied for some spws. The phase-tracking centre was

Table 1. Transitions, their parameters, and spectral window parameters.

Molecule	Transition	ν [a] (MHz)	E_{up} [a] (K)	$S_{ij}\mu^2$ [a] (D^2)	n_{cr} [b] (10^4 cm^{-3})	dV (km s^{-1})	Beam (PA) ($'' \times ''$, $^\circ$)	Chan. rms (mJy beam^{-1})
HC_3N	24–23	218 324.72	131	334.2	8.3	0.5 [c]	0.52×0.29 (−69)	5.4
CH_3OH	$4_{-2,3}-3_{-1,2}$ E	218 440.06	45	13.9	2.2	0.17	0.55×0.29 (−73)	5.5
	$4_{2,3}-5_{1,4}$ A	234 683.37	61	4.5	0.5	0.16	0.49×0.27 (−71)	5.8
	$5_{1,4}-4_{1,3}$ A	243 915.78	50	15.5	1.9	0.15	0.27×0.22 (−95)	4.7
$C^{18}O$	2–1	219 560.35	16	0.02	0.5	0.17	0.53×0.29 (−71)	5.0
CS	5–4	244 935.56	35	19.1	130	0.15	0.33×0.27 (−68)	3.7
CH_3CN	14_1-13_1	257 522.42	100	295.2	9.3	0.42 [c]	0.31×0.26 (−71)	2.8
	14_0-13_0	257 527.38	93	296.7	10.2			
$H^{13}CN$ [d]	J = 3–2, F = 4–3	259 011.86	25	34.4	410	0.45 [d]	0.33×0.27 (−68)	2.1
SiO	6–5	260 518.02	44	57.6	50	0.42 [c]	0.30×0.26 (−73)	2.5
CCH [d]	$N = 3-2$, $J = 5/2-3/2$, $F = 3-2$	262 064.99	25	4.3	6.5	0.42 [c]	0.30×0.26 (−73)	2.5

Notes. [a]Frequencies and spectroscopic parameters have been extracted from the CDMS catalogue (Müller et al. 2001, 2005). [b]The critical densities of CS and $H^{13}CN$ were obtained from Shirley (2015) at 50 K, and those of the other tracers were estimated at 50 K using the LAMDA database (Schöier et al. 2005). [c]The spectral channels of these spws were smoothed by a factor of 3 to gain in signal-to-noise ratio. [d]$H^{13}CN$ and CCH consist of two hyperfine components in 0.4 MHz interval. Those with the higher $S_{ij}\mu^2$ are reported here.

RA (J2000) = $05^h35^m26\overset{s}{.}97$, Dec (J2000) = $-05°09'54\overset{''}{.}50$, and the systemic velocity was set to $V_{LSR} = 11.4$ km s^{-1}. The quasars J0510+1800 and J0522-3627 were used for bandpass and flux calibration, while J0607-0834 and J0501-0159 were used for phase calibration. The absolute flux calibration uncertainty is estimated to be <10%.

The data calibration was performed using the standard ALMA calibration pipeline with the Common Astronomy Software Applications package (CASA[1]; McMullin et al. 2007), while self-calibration, imaging, cleaning, and data analysis were performed using the IRAM-GILDAS software package[2]. The continuum images were produced by averaging line-free channels from the wide spectral windows at 232 GHz and 246 GHz in the visibility plane. The resulting beam size and rms are ($0\overset{''}{.}28 \times 0\overset{''}{.}23$ and 95.7 μJy beam^{-1}) and ($0\overset{''}{.}50 \times 0\overset{''}{.}27$ and 91.7 μJy beam^{-1}). Phase self-calibration was performed on the continuum emission, and the gain solutions were applied to the line cubes. Continuum subtraction was performed on the cubes in the visibility plane before line imaging. The data were cleaned in GILDAS MAPPING using the Clark algorithm (Clark 1980). The resulting synthesised clean beam, velocity resolution, and channel rms for each spectral window are summarised in Table 1. The line identification was performed using the Cologne Database for Molecular Spectroscopy (CDMS[3]; Müller et al. 2001, 2005). The maps shown in the paper are not corrected for the primary beam attenuation because we are more interested in the structure morphology (rather than the flux) that was not affected by the primary beam attenuation. However, we took the correction into account in the spectra.

3. Results

We have imaged the emission from eight different molecules: SiO, CH_3OH, $C^{18}O$, CS, CH_3CN, $H^{13}CN$, HC_3N, and CCH at a high angular and spectral resolution (~$0\overset{''}{.}33$ and ~0.16 km s^{-1}). We mapped three different transitions of CH_3OH and one transition for the other molecules (see Table 1).

[1] https://casa.nrao.edu/
[2] http://www.iram.fr/IRAMFR/GILDAS/
[3] https://cdms.astro.uni-koeln.de

3.1. Spatial distribution of molecular emission

3.1.1. CS and $C^{18}O$

In Fig. 1, we show the velocity-integrated maps[4] of the observed molecular tracers in colours, on which we overlaid CH_3OH ($5_{1,4}-4_{1,3}$ A) contours. CS, a typical high-density tracer ($n_{cr} = 1.3 \times 10^6$ cm^{-3} for the 5–4 transition, see Table 1), shows the brightest and most extended emission in our maps. It probes the overall structures of the gas in the FIR 4 protocluster, a ridge in the east side extending from the north-east (NE) to the south-west (SW, hereafter called eastern ridge), and several filamentary structures. The eastern ridge has a length of ~20″ (~7900 au) and extends over ~3300 au. The other filamentary structures are relatively shorter, with a length ranging between ~4″ and 10″ (~1500–4000 au). $C^{18}O$ traces the eastern ridge, but its emission is less extended (see Sect. 3.2). All the other molecules are emitting from the region covered by CS, except for SiO.

3.1.2. SiO

SiO traces the shocked regions within the FIR 4 protocluster. From the overlap of its velocity-integrated map with the CH_3OH contours, we can notice a different morphology and a shift in the emission. More specifically, two regions of the cloud can be distinguished: a region dominated by SiO located to the west, and another dominated by CH_3OH to the east. Furthermore, SiO reveals multiple bow-shock features: an arc-like extended bow shock to the west of the cluster (hereafter called Arc 1) and a smaller bow shock located south-west of the cluster (hereafter called arc 2). Arc 1 extends over ~2700 au, while arc 2 extends over ~500 au. SiO emission had already been reported towards the west of FIR 4 region, but at lower angular resolution (~3″−7″; Shimajiri et al. 2008). In addition, we report a collimated monopolar molecular jet from the protostar VLA15. The jet extends along the S-N direction, with a length of 13.3″

[4] The maps were integrated between the following ranges: 7.4 and 15.4 km s^{-1} for $C^{18}O$, –0.2 and 24.4 km s^{-1} for CS, –6.2 and 24.4 km s^{-1} for SiO, 3.4 and 19.4 km s^{-1} for CH_3OH, 7.6 and 23.6 km s^{-1} for CH_3CN, 1.5 and 21.8 km s^{-1} for $H^{13}CN$, 5 and 21.4 km s^{-1} for HC_3N, and 2.1 and 20.6 km s^{-1} for CCH.

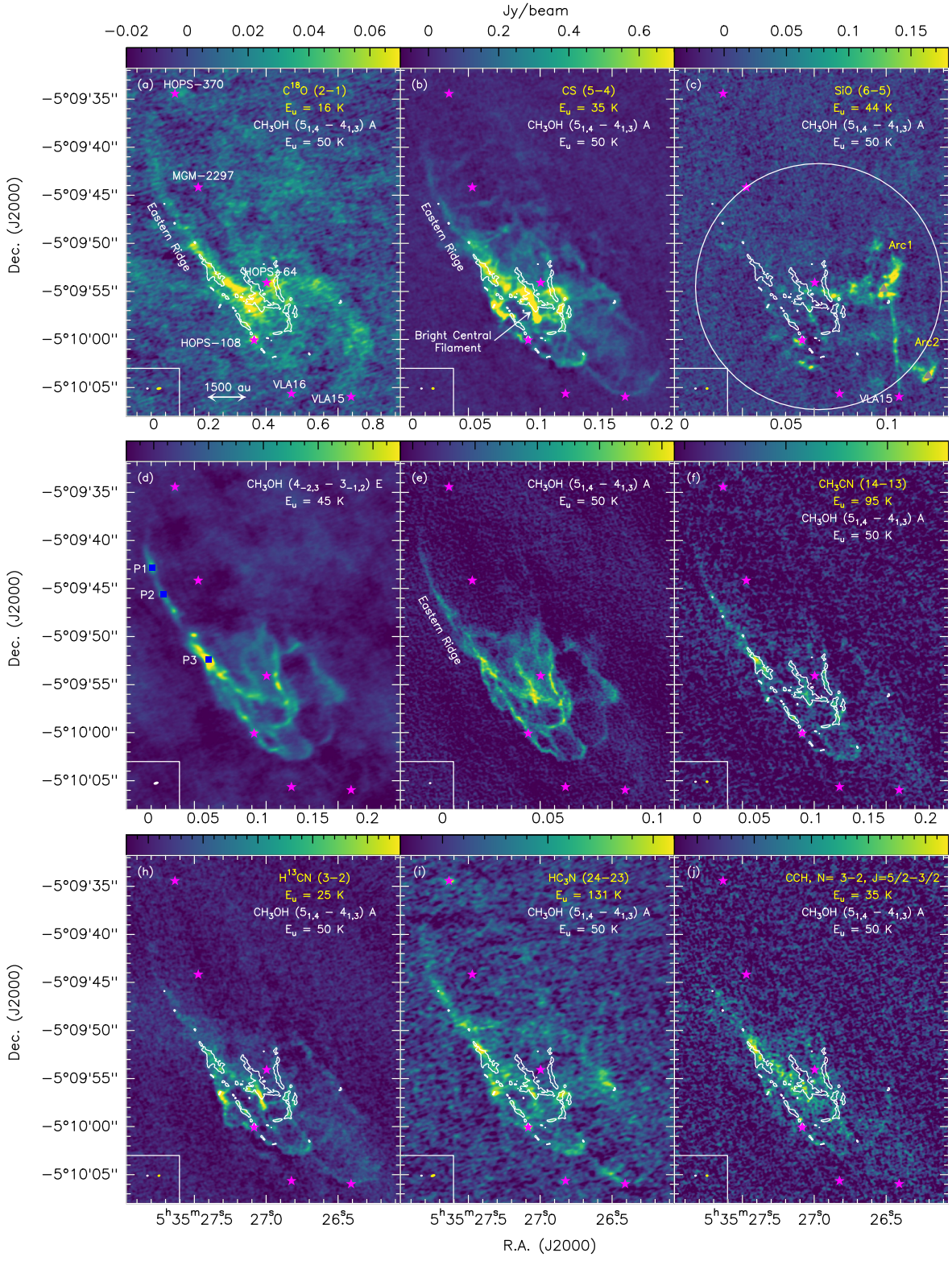

Fig. 1. Velocity-integrated maps of the different tracers used to probe the emission towards OMC-2 FIR 4. *Upper panels*: velocity-integrated maps of $C^{18}O$, CS and SiO in colours, with superimposed contours of the velocity-integrated emission of CH_3OH ($5_{1,4}$−$4_{1,3}$ A) line (white). The colour scale wedges are shown at the top of each panel. The different cores are depicted with magenta stars and are labelled in white. The synthesised beam of CH_3OH and the other molecules are depicted in the lower left corner in white and yellow, respectively. In the SiO panel, the positions of the SiO peaks from this study are depicted with filled grey triangles. The primary beam at the full width at half maximum is depicted in white. *Middle panels*: velocity-integrated maps of CH_3OH lines at E_u = 45 K and E_u = 50 K and of CH_3CN. On the latter, we superimposed the contours of the velocity-integrated emission of CH_3OH ($5_{1,4}$−$4_{1,3}$ A) line (white). The colour scale wedges are shown at the top of each panel. The positions of the three masers detected in CH_3OH ($4_{-2,3}$−$3_{-1,2}$ E) are depicted with filled blue squares. *Lower panels*: velocity-integrated maps of $H^{13}CN$, HC_3N and CCH in colours with superimposed contours of the velocity-integrated emission of CH_3OH ($5_{1,4}$−$4_{1,3}$ A) line (white). The colour scale wedges are shown at the top of each panel. The methanol contours start at 10σ with $\sigma = 12.3$ mJy beam^{-1} km s^{-1}.

Table 2. Position of the detected CH_3OH ($4_{-2,3}-3_{-1,2}$ E) maser spots along the eastern ridge.

Spot	RA(J2000) ($^h\,^m\,^s$)	Dec(J2000) ($^\circ\,'\,''$)
P1	05:35:27.792	−05:09:42.82
P2	05:35:27.717	−05:09:45.62
P3	05:35:27.401	−05:09:52.38

(∼5200 au). The source driving the jet was recently identified as a young and deeply embedded protostar (Osorio et al. 2017; Tobin et al. 2019) that appears to have an edge-on horizontal disk (Tobin et al. 2019). The class of this protostar has not yet been determined.

3.1.3. CH_3OH

Similarly to CS, the CH_3OH velocity-integrated maps shown in the middle panel of Fig. 1 reveal several cavities from NE to SW and widespread interwoven filamentary structures. The origin of these structures is discussed in Sect. 4.1.

For the CH_3OH ($4_{-2,3}-3_{-1,2}$ E) transition, known to be a class I-type CH_3OH maser (Hunter et al. 2014; Chen et al. 2019), we noted that in three positions (P1, P2, and P3) along the eastern ridge (see panel (d) in Fig. 1), the line intensities were >300 K km s^{-1}. This suggests the presence of maser spots at these positions. Maser spots were previously identified at the same position, with different CH_3OH maser transitions (e.g. Kogan & Slysh 1998; Kang et al. 2013; Fontani et al., in prep.). The maser at P2 was observed at 7 mm, 3 mm, and 2 mm (Kang et al. 2013), while those at P1 and P3 were observed at 3 mm (Fontani et al. in prep.). Hence, we report the detection of these masers at 1 mm. The locations of the maser spots we detect along the eastern ridge are reported in Table 2. The narrow spectra extracted at the peak of the above-mentioned spots are shown in Fig. A.1. It is worth noting that on one hand, the class I-type CH_3OH masers result from collisional pumping (e.g. Sobolev et al. 2007; Ladeyschikov et al. 2020; Nesterenok 2022), which can be associated with young stellar object outflows (Voronkov et al. 2006; Chen et al. 2011; Ladeyschikov et al. 2020), expanding H II regions (Voronkov et al. 2014), expanding supernova remnants (Pihlström et al. 2014), and rapidly moving cloudlets (Voronkov et al. 2010). Hence, they indicate the presence of compressed gas. On the other hand, Kang et al. (2013) suggested that the exciting source of the maser at P2 could be one of the protostars in the OMC-2 FIR 3/4 clusters, and Osorio et al. (2017) have reported radio emission associated with the jet from the protostar HOPS-370 close to the maser at P3.

We detected three CH_3OH lines with close upper state energies. Therefore, we were not able to perform a non-local thermodynamic equilibrium analysis (non-LTE).

3.1.4. $H^{13}CN$, CH_3CN, HC_3N, CCH, and dust

The emission of $H^{13}CN$, CH_3CN, HC_3N, and CCH is fainter, but agrees reasonably well with the CS and CH_3OH morphology. The eastern ridge is detected in all the tracers. The hot corino HOPS-108 (Tobin et al. 2019; Chahine et al. 2022) is also observed in all the molecules except for CCH, which is a traditional probe of UV illuminated regions (e.g. Gratier et al. 2017; Bouvier et al. 2020). Moreover, the bright central filament (∼4″ in length) probed by CS is very well detected in $H^{13}CN$, the other tracer of high-density gas ($n_{cr} = 4.1\times10^6$ cm^{-3} for the 3–2 transition, see Table 1), suggesting that this filament might be one of the densest within the protocluster.

Finally, in addition to probing the protostars within OMC-2 FIR 4, the continuum emission also traces some filamentary structures. The overall distribution of CH_3OH emission follows the filament morphology observed in the continuum (see Fig. 2). The eastern ridge is well probed by dust emission, suggesting that it is in high-density conditions.

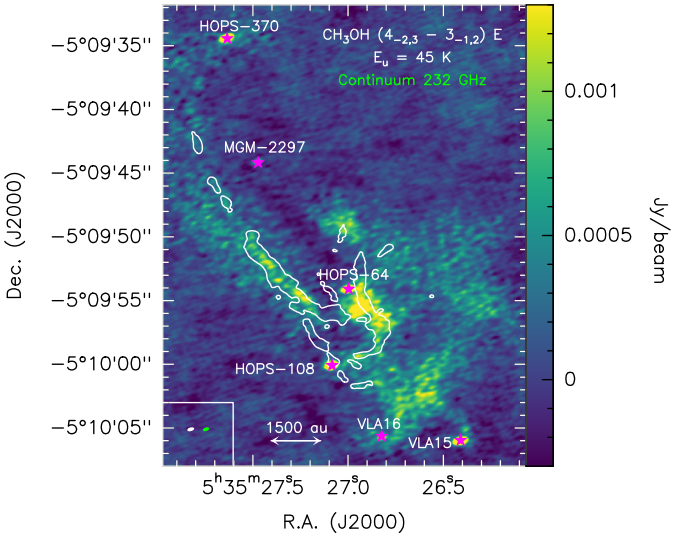

Fig. 2. Continuum emission towards OMC-2 FIR 4 at 232 GHz in colours, with superimposed contours of the velocity-integrated emission of CH_3OH ($4_{-2,3}-3_{-1,2}$ E) at 15σ with σ = 20.6 mJy beam^{-1} km s^{-1}. The different cores are depicted with magenta stars and are labelled in white. The synthesised beam of CH_3OH and continuum are depicted in the lower left corner in white and green, respectively.

3.2. Kinematics of molecular emission

We provide velocity maps (moment 1) and velocity–dispersion maps (moment 2) for CH_3OH and SiO (Figs. 3 and 4). We also show the velocity channel maps for CH_3OH, $C^{18}O$, HC_3N, CS, and SiO (see Figs. C.2–C.6). $C^{18}O$ and CS are plausibly affected by missing flux due to structures larger than the maximum recoverable scale (MRS∼11.″2). Therefore, we did not analyse the kinematics using these tracers. The remaining molecular tracers are either faint or have a hyperfine structure, hence the study of their kinematics would not be reliable.

The average systemic velocity of the FIR 4 protocluster is V_{sys} = 11.4 km s^{-1} (Shimajiri et al. 2008; Favre et al. 2018). Remarkably, from the velocity maps and channel maps of CH_3OH, we can clearly see that each filament has a different velocity and that the filaments at the centre of the cloud have higher velocities (>2 km s^{-1}) than the external filaments in both red- and blueshifted emission. The velocity gradient in CH_3OH between the east and the west of the FIR 4 protocluster is about ±4 km s^{-1} with respect to the systemic velocity. From the velocity-dispersion maps of CH_3OH in Fig. 4, it seems that we have three distinct spatial distributions of the velocity dispersion:

1. The external filamentary structures that have the lowest velocity dispersion, <2 km s^{-1}.
2. The intermediate filaments around the central region that have a velocity dispersion of 2–4 km s^{-1}.

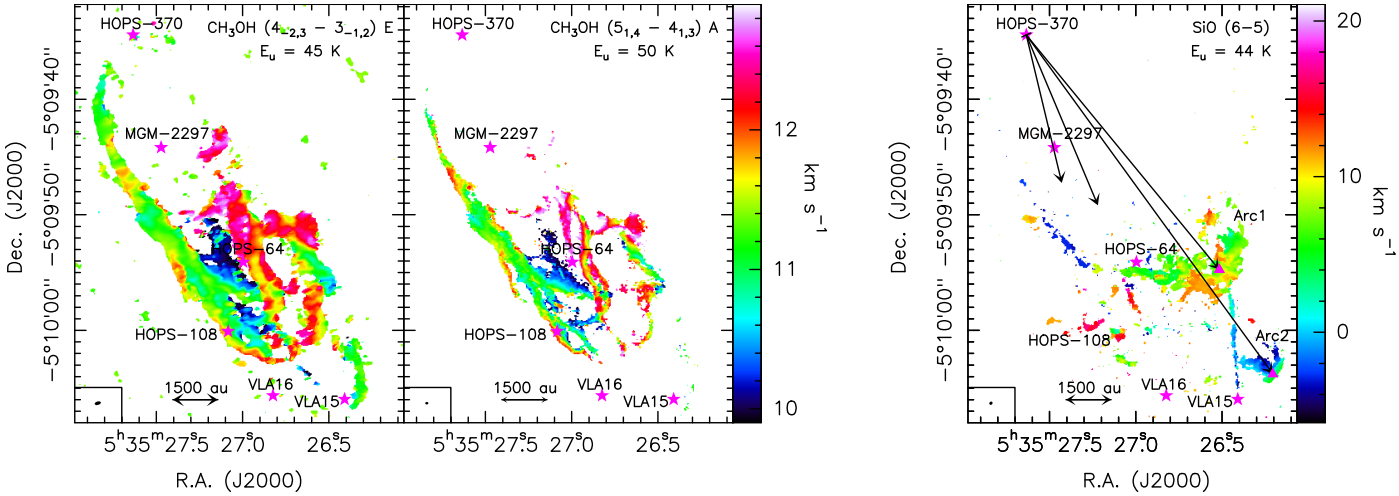

Fig. 3. Velocity maps of CH_3OH and SiO towards OMC-2 FIR 4. *Left panel*: velocity maps (integrated between 9.9 and 12.9 km s^{-1}; colour scale in km s^{-1}) of CH_3OH ($4_{-2,3}$−$3_{-1,2}$ E) (*left*) and CH_3OH ($5_{1,4}$−$4_{1,3}$ A) (*right*). *Right panel*: velocity map (integrated between –6.2 and 24.4 km s^{-1}; colour scale in km s^{-1}) of SiO(6–5). The different cores are depicted with magenta stars and are labelled in black. The positions of the SiO peaks from this study are depicted with filled magenta triangles. We draw four arrows from HOPS-370, one perpendicular to the disk, two towards the SiO peaks, and one similar to the direction of the jet in [O I] by González-García et al. (2016).

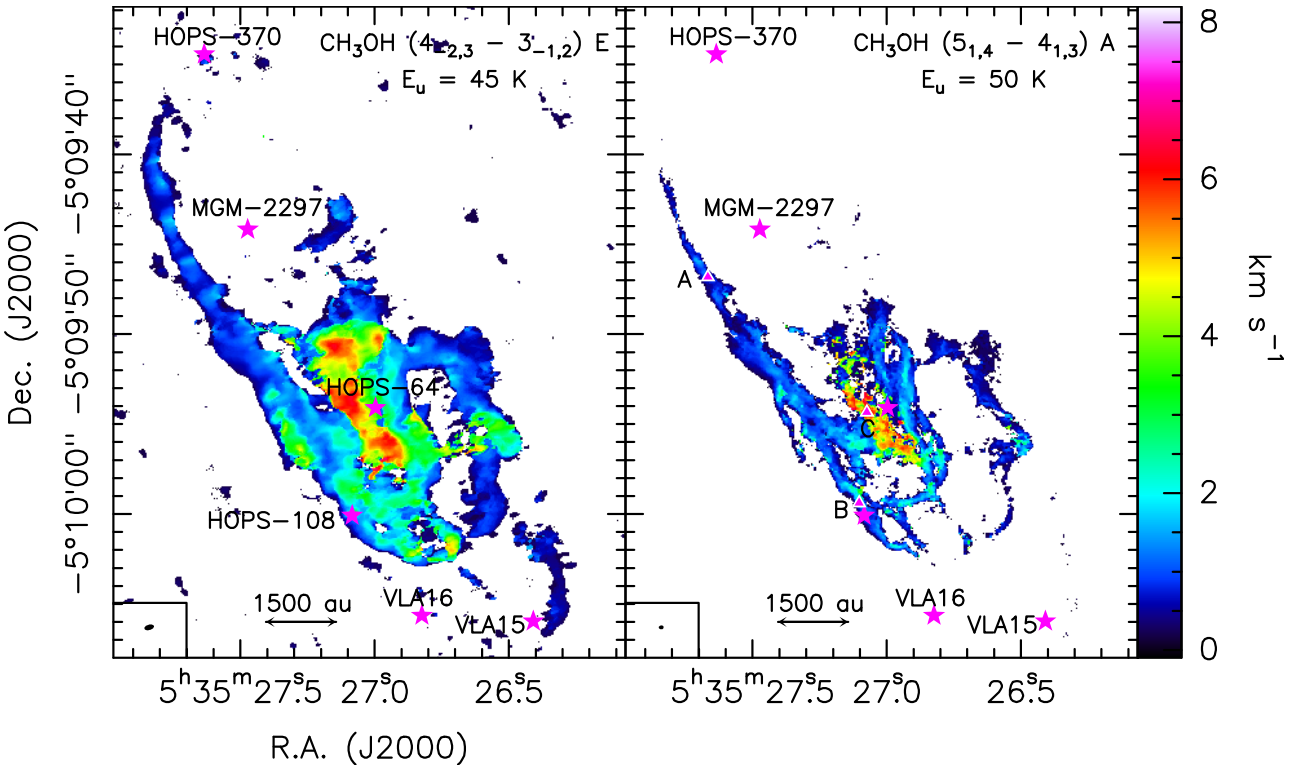

Fig. 4. Velocity–dispersion maps (integrated between 7.4 and 15.4 km s^{-1}; colour scale in km s^{-1}) of CH_3OH ($4_{-2,3}$−$3_{-1,2}$ E) (*left*) and CH_3OH ($5_{1,4}$−$4_{1,3}$ A) (*right*). The positions (A, B, and C) from which we extracted the spectra in Fig. A.2 are labelled with filled magenta triangles.

3. The central region showing (in the moment 2 map) a velocity dispersion of 4–7 km s^{-1}.

However, the high dispersion in the central region is actually due to the presence of multiple structures along the line of sight (see Fig. A.2). In Fig. A.2, we show the spectra extracted from three different positions that are marked by magenta triangles in the moment2 map.

A completely different velocity distribution is observed in SiO. Its emission extends up to much higher blueshifted velocities than the other tracers, covering a wide velocity range of $-17.6 < V–V_{sys} < +8$ km s^{-1}. From the SiO velocity and channel maps, three velocity regimes with different spatial distribution can be identified:

1. Blueshifted high-velocity (HV) regime in the range $-17.6 < V–V_{sys} < -8.1$ km s^{-1}, where SiO reveals the decelerating jet from VLA15, the south-west bow-shock (arc 2) and the elongated eastern ridge.
2. Blueshifted low-velocity (LV) regime in the range $-8 < V–V_{sys} < 0$ km s^{-1}, where SiO probes the extended arc-like bow (arc 1) west of the cluster.

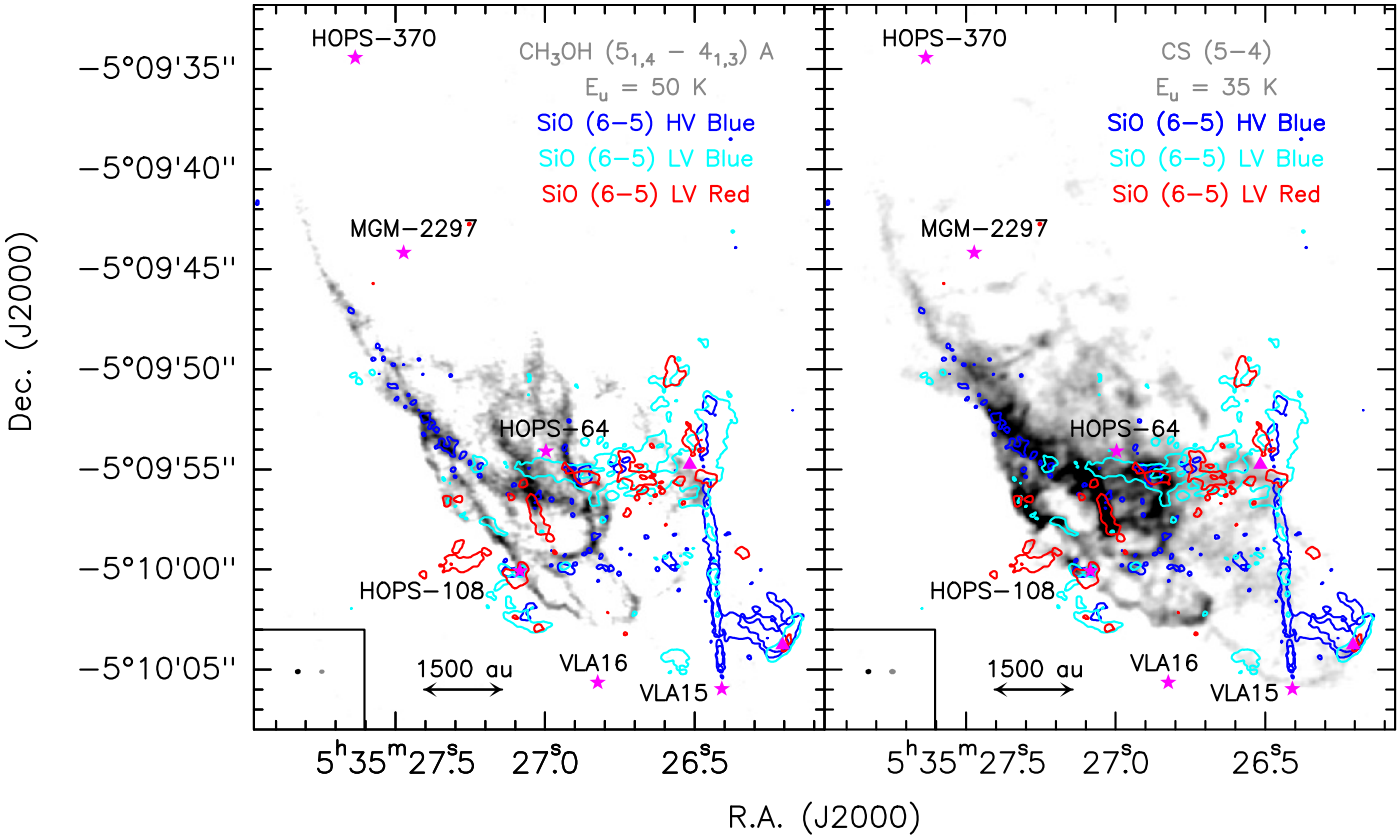

Fig. 5. Velocity-integrated maps of CH_3OH and CS reported in Fig. 1 with superimposed contours of the velocity-integrated emission of SiO at different velocity regimes. The colour images are as in Fig. 1. The SiO contours are at 5σ with $\sigma = 5.8$ mJy beam^{-1} km s^{-1}. They correspond to the blueshifted high-velocity regime (blue), the blueshifted low-velocity regime (white), and the redshifted low-velocity regime (red) (see Sect. 3.2). The different cores are depicted with magenta stars and are labelled in black. The positions of the SiO peaks from this study are depicted with filled magenta triangles.

3. Redshifted low-velocity (LV) regime in the range $+0.1 < V - V_{sys} < +8$ km s^{-1}, where SiO probes more compact filaments than the blueshifted parts.

It is worth noting that the redshifted counterpart of the jet from VLA15 is not detected in our data as it is ∼3″ out of our primary beam. However, the possibility of having a monopolar jet cannot be excluded (e.g. Codella et al. 2014). Interestingly, the jet can also be observed in CS at high blueshifted velocities in the range $-0.2 < V < +3.3$ km s^{-1} (see the bottom left panel in Fig. C.5).

We overlaid the integrated contours of each velocity regime on the velocity-integrated maps of CH_3OH, CS, and $H^{13}CN$ (see Fig. 5). We note that the bow shocks in SiO are spatially unrelated to the bulk emission that is traced by the other molecules, but SiO traces some filamentary structures within OMC-2 FIR 4 at certain velocities. At higher blueshifted velocities (HV) SiO traces the eastern ridge, which is probed by all the other molecular tracers and by the dust emission. It also traces the filamentary structure located west of the protostar HOPS-64 and the cavity located west of the source HOPS-108. While in the red LV regime, SiO probes the central collimated filament, which is also observed in CS and $H^{13}CN$. The detection of SiO in some filamentary structures indicates that these filaments contain shocked gas, where the gas is compressed and warmed up. This is also confirmed by the detection of the class-I CH_3OH maser spots along the eastern ridge.

4. Discussion

4.1. Origin of the filaments

At ∼1 pc scale and ∼1800 au angular resolution, Hacar et al. (2018) identified 55 fibres along the OMC-1 and OMC-2 clouds of the ISF using the quiescent gas tracer N_2H^+. They have suggested that the fibres towards the OMC-1 south region, the OMC-1 ridge, and towards the centres of OMC-2 FIR 4 and OMC-2 FIR 6 are distributed in fan-like arrangements, while they are sparse outside these regions (see their Sect. 3.5). Furthermore, they noted that the fibre hubs coincide with the positions of different (stars plus gas) mass concentrations along the ISF. The algorithm HiFive used in their study was not able to decompose the most complex structures, such as OMC-2 FIR 4, which consists of multiple sub-branches. However, one main fibre within this region was clearly identified in their study, and it is fibre number 43 (see their Fig. 4).

Our observations of the OMC-2 FIR 4 protocluster at a spatial resolution of ∼100 au reveal a collection of intertwined filamentary structures within a field of view of ∼10 000 au. To assess whether these structures are associated with the fibres observed with N_2H^+ at larger scales, we superimposed the CH_3OH ($5_{1,4}$–$4_{1,3}$ A) and CS contours emission from our work on the N_2H^+ (1–0) emission map from Hacar et al. (2018) (see Fig. 6). This figure shows that N_2H^+ emission surrounds that of CH_3OH and CS. Our eastern ridge is aligned with fibre 43 iden-

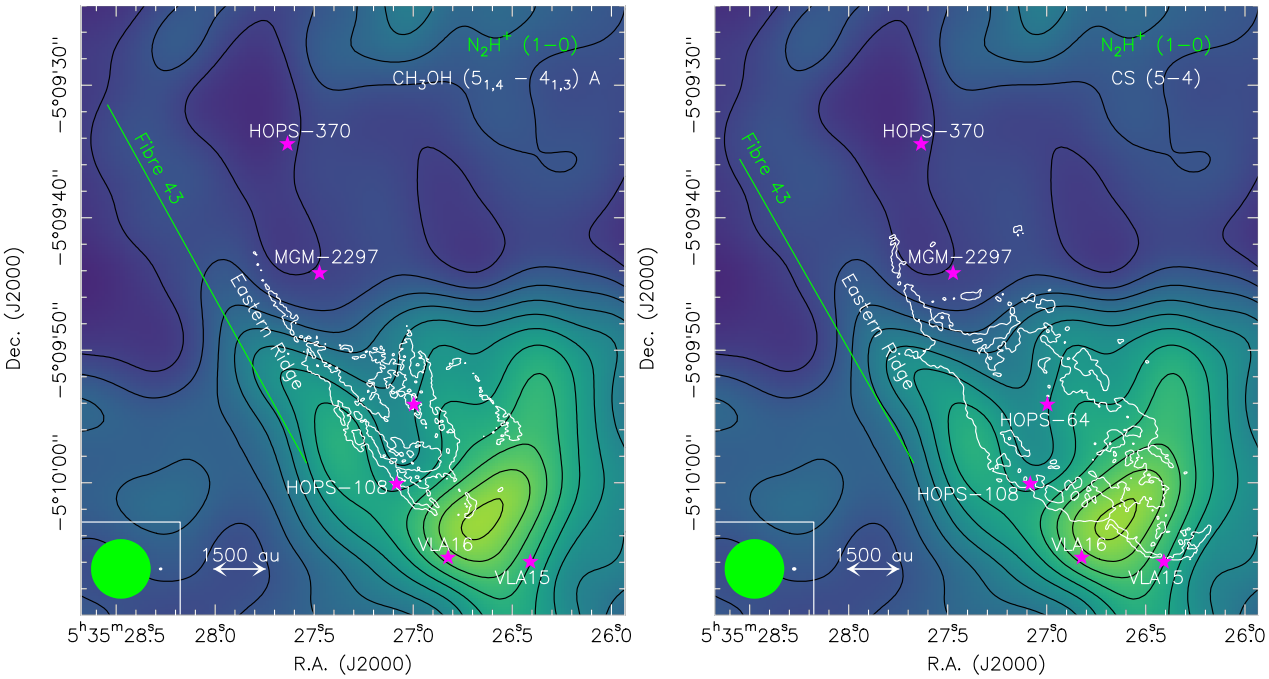

Fig. 6. N_2H^+(1–0) integrated intensity emission from Hacar et al. (2018) in colour scale and black contours, with superimposed 5σ contours of the velocity-integrated emission of CH_3OH ($5_{1,4}$–$4_{1,3}$ A) (*left*) and CS (*right*) from this work. N_2H^+ contours are equally spaced every 1 Jy beam^{-1} km s^{-1}. The CH_3OH and CS contours are shown at 5σ with σ = 12.3 mJy beam^{-1} km s^{-1} and 23.2 mJy beam^{-1} km s^{-1}, respectively. The different cores are depicted with magenta stars and are labelled in white. The direction of Fibre 43 is shown with a green line. The synthesised beams of N_2H^+, CH_3OH (*left*), and CS (*right*) are depicted in the lower left corner in green and white, respectively.

tified by Hacar et al. (2018). The other shorter filaments could be connected to the multiple sub-branches of the fibres' hub that were not recovered by HiFive. Taking into account the differences in scales, angular resolution, and tracers, we can say that the two works are complementary. Whereas at 4.5″, Hacar et al. (2018) observed the dense fibres, the higher angular resolution have allowed us to resolve the filamentary structures within the hub. In addition, CH_3OH has offered us a probe of the dynamics. While with N_2H^+ the centroid velocities $V_{LSR}(N_2H^+)$ of the fitted components in OMC-2 FIR 4 region range from ∼10 to 12.5 km s^{-1} from east to west with a velocity dispersion between 0.2 and 2.2 km s^{-1} (see their Fig. B.3), our CH_3OH filamentary structures show a higher velocity dispersion, ranging between 0.9 and 3.2 km s^{-1} (excluding the line width of maser spots). Each of the CH_3OH filaments has a different velocity, with those at the centre being higher (V ∼ 7.4 km s^{-1} for the most blueshifted filament and V ∼ 17.4 km s^{-1} for the most redshifted one). The velocity range and dispersion are indicative of supersonic motions within the protocluster. To verify this point, we compared the magnitude of the line-of-sight non-thermal velocity dispersion σ_{NT} with the local thermal sound speed of H_2, $c_s(T_K)$ (e.g. Hacar & Tafalla 2011; Hacar et al. 2018). We used the ratio $\sigma_{NT}/c_s(T_K)$ to identify whether the observed gas motions are subsonic ($\sigma_{NT}/c_s(T_K) \leq 1$), transonic ($1 < \sigma_{NT}/c_s(T_K) \leq 2$), or supersonic ($\sigma_{NT}/c_s(T_K) > 2$) (Hacar et al. 2018, 2022). The line width of a spectrum combines contributions from both thermal and non-thermal gas motions. Consequently, to estimate the non-thermal component σ_{NT}, we subtracted the thermal component from the measured line width of the spectra, assuming that the two contributions are independent of one another (Myers 1983),

$$\sigma_{NT} = \sqrt{\frac{\Delta V^2}{8 \ln 2} - \frac{k_B T_K}{\mu_{(CH_3OH)}\, m_p}}. \quad (1)$$

Thus, for line widths of [0.9–3.2 km s^{-1}] as obtained from our spectra, σ_{NT} will range between ∼0.4 and 1.4 km s^{-1}. On the other hand, for an isothermal medium, $c_s(T_K)$ is given as

$$c_s(T_K) = \sqrt{\frac{k_B T_K}{\mu_{(H_2)}\, m_p}}. \quad (2)$$

The kinetic temperature of the gas within OMC-2 FIR 4 was estimated to be ∼40 K (Favre et al. 2018), so $c_s(T_K)$ is ∼0.4 km s^{-1}. Hence, the ratio $\sigma_{NT}/c_s(T_K)$ of the filamentary structures ranges between ∼1 and 3.3, implying the presence of transonic and supersonic motions. As proposed by Henshaw et al. (2014) for the infrared dark cloud (IRDC) G035.39-00.33, we suggest that the kinematics of the filamentary structures could be affected by the outflows from the forming stars within the protocluster. Gaseous CH_3OH and CS would testify to a recent injection or formation of these species into the gas-phase, which have not yet had the time to accrete onto the grain mantles. For a density of about 10^5 cm^{-3}, the timescale for methanol accretion is about 10^4 yr, and this timescale is slightly longer for CS. This supports the idea that what we see within OMC-2 FIR 4 could be the result of the protostellar feedback (i.e. outflows, winds, and radiation) that shaped the material in filament-like structures. Hence, the results highlight the importance of stellar feedback on the evolution of molecular hubs, where the material can be shaped and compressed within narrow filaments.

4.2. SiO fingerprint in filaments

Another key molecule we detect along some of the filamentary structures is SiO (see Fig. 5). Figure 5 shows the detection of SiO along three filamentary structures: the eastern ridge, the filament located west of the protostar HOPS-64, and the central collimated filament. Its detection in the filamentary structures

indicates that the gas is compressed and possibly shocked. The shocks could be induced by internal or external feedback processes. For example, the detection of narrow widespread SiO emission at parsec scale in high-mass star-forming filaments was thought to be caused by either gentle filament merging, that is, merging occurring at relatively low velocity (Jiménez-Serra et al. 2010; Henshaw et al. 2013), or by a decelerated shocked gas associated with large-scale outflows driven by the protostellar sources (Jiménez-Serra et al. 2010; López-Sepulcre et al. 2016). Higher-resolution studies have added a new possibility, which is the collision between the star-forming cloud and the molecular gas pushed by H II regions or supernova remnants (e.g. Cosentino et al. 2019, 2020). Recently, both SiO and CH_3OH emission were observed at sub-parsec scales and ~2″ angular resolution in the filamentary structures of IRAS 4, a low-mass protostellar system located in the NGC 1333 star-forming region (De Simone et al. 2022). The authors suggested that the emission arises from shock trains due to an expanding gas bubble, coming from behind NGC 1333 and clashing against the filament, where IRAS 4A lies. The narrow (<2 km s^{-1}) SiO HV imprint along the eastern ridge (see Fig. A.3) suggests that a similar scenario cannot be excluded in our case. Several molecular CO shells from B stars were observed in the surroundings of OMC-2 FIR 4 (Feddersen et al. 2018), in addition to an increase of CO emission at the eastern edge of the ISF (Shimajiri et al. 2011). Hence, the shocks in the filamentary structures of OMC-2 FIR 4 may be induced by the compression of the cloud due to some external mechanisms such as an expanding bubble that impact the protocluster or external winds from the OB stars located nearby. Alternatively, the SiO signature along the filamentary structures can be produced by the feedback of the protostars within the cluster, as discussed in the previous section. The coincidence of SiO with dust emission (see Fig. C.1) could be indicative of dense or compressed gas that is not necessarily shocked. This is also consistent with the detection of the class I type CH_3OH masers along the eastern ridge. To comprehend which feedback process might be compressing the cluster and producing the SiO along the filamentary structures, we need to observe more molecular line transitions to derive the SiO abundance and the gas physical properties. An alternative interpretation of the SiO blueshifted emission along the eastern ridge is discussed in Sect. 4.4.

4.3. SiO jet from VLA15

Figure 7 presents the SiO(6–5) clumpy elongated jet from VLA15. The jet is very narrow and shows a wiggle, similarly to what has been reported in HH212, another protostar located in Orion (Lee et al. 2015, 2017). To investigate the jet collimation, we measured the width along several cuts perpendicular to the jet axis where the SiO emission is >10σ. The widths were measured by fitting the spatial profile of each cut with a Gaussian profile. Then the deconvolved widths were derived by correcting the full width at half maximum (FWHM) of the observed emission for the size of the beam perpendicular to the jet axis employing the same equation as was used by Podio et al. (2021). We plot the deconvolved sizes as a function of the distance from VLA15 in Fig. 8. The width increases slightly with the distance. At 600–800 au from the source, the widths were estimated to be ~35–60 au, slightly lower than the width of HH212 jet estimated at the same distances (~80 au; Cabrit et al. 2007). We derived the average collimation angle of the VLA15 jet by fitting the measured cut widths with a straight line, taking the measurement errors into account. We performed the fit using the Python

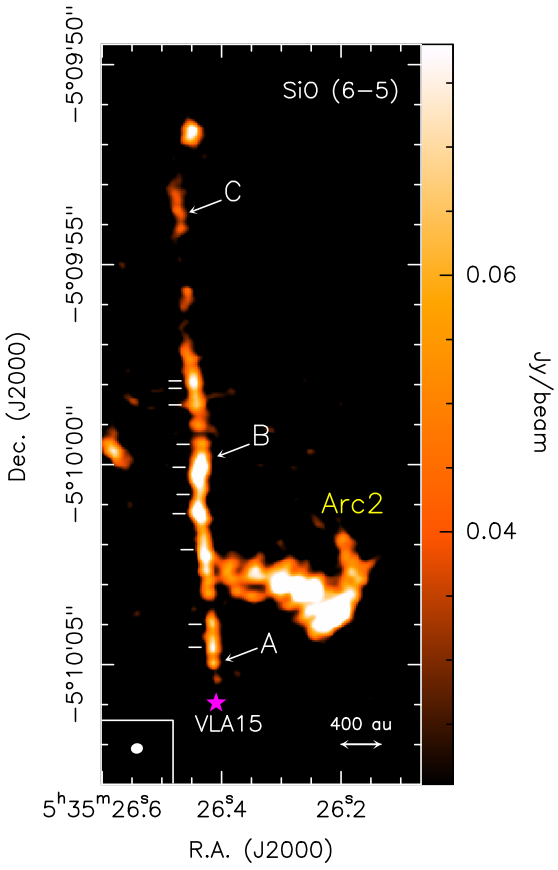

Fig. 7. Velocity-integrated emission of the SiO jet driven by VLA15. The colour images are for intensities higher than 3σ with σ = 4.8 mJy beam^{-1} km s^{-1}. The cut positions at which the widths were measured are shown with white horizontal lines. The knot positions at which the dynamical ages are estimated are shown with arrows and are labelled in white. VLA15 is depicted with a magenta star and labelled in white. The synthesised beam is depicted in the lower left corner.

function *curve_fit*, according to the following equation:

$$2R_{\rm jet} = 2\,\tan(\alpha/2)z + 2R_0, \quad (3)$$

where $2R_{\rm jet}$ is the deconvolved width, z is the distance from the source VLA15, α is the apparent full opening angle of the flow[5], and R_0 is a constant offset. For reference, we drew a dashed green line that represents a collimation with a full opening angle of α = 3° and initial width of 30 au, as was done by Podio et al. (2021). Our estimated widths fall below this line. We derived an apparent full opening angle α = 0.9° ± 0.5° from the fit, indicating that the jet of VLA15 is highly collimated (<2°). The jet collimation agrees with the values derived for atomic jets from class II sources (~3°), while it is smaller than those inferred for the class 0 SiO jets of the CALYPSO survey (4°–12° at >300 au distances; Podio et al. 2021). Our value is also lower than the value inferred for HH212 IRAM-PdBI observations (Codella et al. 2007; Cabrit et al. 2007), possibly due to the lower spatial resolution (~150 au). The very small opening angle that we derive (~1°) indicates that at the distance of the closest detected knot (~600 au) the jet is already collimated. Hence, our results suggest the VLA15 SiO jet is one of the

[5] Due to projection effects, the true opening angle is smaller: $\tan(\alpha_{\rm true}) = \tan(\alpha) \times \sin(i)$, where i is the inclination with respect to the line of sight.

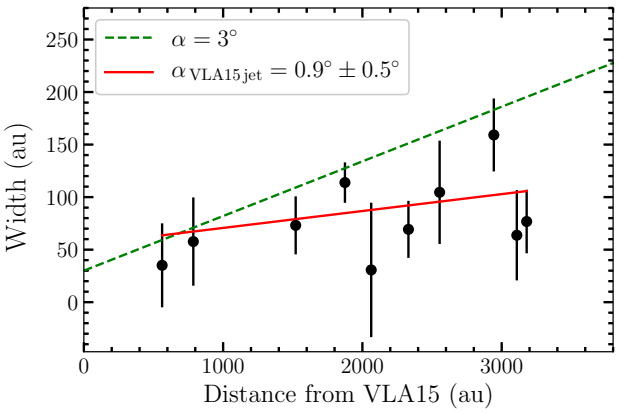

Fig. 8. Deconvolved widths ($2R_{\rm jet}$) of the SiO(6–5) emission along the jet axis as a function of the distance from VLA15. The solid red line corresponds to the best fit of the data points. The dashed green line corresponds to an opening angle of $\alpha = 3°$ and an initial width of 30 au.

most highly collimated jets observed so far. This is consistent with theoretical predictions that jets of young stellar objects are driven by magnetohydrodynamic (MHD) mechanisms (Ray & Ferreira 2021). We verified that the narrow opening angle of the jet is not the result of interferometric filtering by modelling the interferometer response to simulated structures with widths ranging from 1/6 to 10 times the size of the synthesised beam. The widths of the structures were not narrowed, but rather conserved, indicating that they were not resolved out by the interferometer (see Appendix B). Hence, the jet width we observe is real, as is the narrow opening angle we derived.

We estimated the dynamical age of three knots (A, B, and C; see Fig. 7) along the jet assuming again a jet velocity $V_{\rm jet} = 100\,{\rm km\,s^{-1}}$ (Podio et al. 2021). The disk associated with VLA15 appears to be nearly edge-on (Osorio et al. 2017; Tobin et al. 2019), hence its jet likely lies close to the plane of sky ($i = 0°$). In this case, the distances between VLA15 and knots A, B, and C would be $d_{\rm (A)} \sim 420$ au, $d_{\rm (B)} \sim 2260$ au, and $d_{\rm (C)} \sim 4795$ au, respectively. Therefore, the dynamical ages would be $\tau_{\rm (A)} \sim 20$ yr, $\tau_{\rm (B)} \sim 107$ yr, and $\tau_{\rm (C)} \sim 227$ yr. If the jet is inclined with respect to the plane of sky by 30° at most, the dynamical ages of the knots may be older than what was estimated assuming $i = 0°$ by 16% at most.

We note that the radial velocity of the jet goes from $V \sim -6.2\,{\rm km\,s^{-1}}$ to $V \sim +5.4\,{\rm km\,s^{-1}}$ (see Fig. 3). This might be due either to deceleration from an interaction with the material within the FIR 4 cloud and/or to a change in jet direction with respect to the line of sight. The high-velocity dispersion, observed to the south of arc 1 along the direction of the jet from VLA15, suggests that it could be interacting with this bow-shock.

4.4. Possible role of the outflow from HOPS-370

To the north of the OMC-2 FIR 4 region lies the intermediate-mass protostar HOPS-370. This source has a rotating disk with an east-west velocity gradient. It also drives a high-velocity outflow going from $-56\,{\rm km\,s^{-1}}$ to $66\,{\rm km\,s^{-1}}$ with respect to the HOPS-370 systemic velocity (Tobin et al. 2019). The outflow extends from the north-east (NE) to the south-west (SW) of HOPS-370, and it was observed down to ∼0.09 pc south of HOPS-370 (Shimajiri et al. 2008). It was identified through many outflow tracers such as CO (Aso et al. 2000; Williams et al. 2003; Shimajiri et al. 2008, 2015; Wu et al. 2005; Takahashi et al. 2008; González-García et al. 2016; Tobin et al. 2019), HCO^+ (Aso et al. 2000; Shimajiri et al. 2015), CS, HCN (Shimajiri et al. 2015), and [O I] (González-García et al. 2016). It was also observed with VLA at 9 mm and 5 cm by Tobin et al. (2019) and Osorio et al. (2017), respectively. The blue- and redshifted components of the outflow are observed in both directions (Aso et al. 2000; Takahashi et al. 2008; Shimajiri et al. 2008; Tobin et al. 2019). Some authors argued that the outflow directly interacts with clump FIR 4 and triggers the star formation within it (e.g. Shimajiri et al. 2008, 2015; Manoj et al. 2013; González-García et al. 2016; Osorio et al. 2017), while others excluded interaction and suggested that spatial coincidence between the outflow from HOPS-370 and clump FIR 4 is a projection effect (Favre et al. 2018).

The jet driven by HOPS-370 is likely precessing because the direction of the jet detected in [O I] by González-García et al. (2016) is not coincident with that of the 9 mm jet, nor with the axis of outflow cavities detected in CO, which are perpendicular to the disk of HOPS-370 (Tobin et al. 2019). This precession pattern is also supported in our work by the detection of two bright arcs seen in SiO emission, called arc 1 and arc 2. In Fig. 3, we draw arrows along the directions of the [O I] jet, the axis of the outflow cavities seen in CO, and the SiO peaks on the bow-shock features revealed by our observations. The SiO moment 0 and 1 maps show multiple bow-shock features at different velocities, whose emission is not associated with that of the continuum, nor with that of the other tracers (see Figs. 1 and C.1). The geometry of the bow shocks suggests that this is due to a jet activity from HOPS-370. More precisely, the bow shocks might be the signature of a precessing jet that extends from east to west. Hence, the western part of the protocluster is affected by the mass loss arriving from the north. Furthermore, SiO leaves a narrow-line imprint along the eastern ridge. This may be induced by one of the processes discussed in the previous section (i.e. gentle filament merging, winds from nearby H II regions, expanding shells, or stellar feedback). Alternatively, the jet from HOPS-370 may have also contributed to compress and shock the filamentary structures in the protocluster. Nonetheless, due to the limited number of molecular lines in our dataset, we were not able to prefer one of the two different scenarios.

In this paragraph, we estimate the dynamical ages of the arc 1 and arc 2 bow-shocks. The jet is thought to lie close to the plane of the sky (González-García et al. 2016; Tobin et al. 2019). When we consider the CO jet radial velocity (∼50–60 $\rm km\,s^{-1}$) derived by Tobin et al. (2019) and assume a typical jet velocity $V_{\rm jet} = 100\,{\rm km\,s^{-1}}$ (Podio et al. 2021), the inclination angle would be $i < 30°$ with respect to the plane of the sky. If the jet lies on the plane of the sky ($i = 0°$), the distance between HOPS-370 and the SiO peak in arc 1 and arc 2 would be $d_{\rm (Arc\,1)} \sim 10330$ au and $d_{\rm (Arc\,2)} \sim 14150$ au. Hence, the dynamical ages would be $\tau_{\rm (Arc\,1)} = d_{\rm (Arc\,1)}/V_{\rm jet} \sim 490$ yr and $\tau_{\rm (Arc\,2)} \sim 670$ yr, respectively. The jet may be inclined with respect to the plane of the sky by 30° at most, which implies that the shock dynamical ages may be older than what was estimated assuming $i = 0°$ by 15% at most. The fact that arc 2 is older than arc 1 suggests that the jet of HOPS-370 is precessing from east to west and then proceeds away.

Interestingly, the outflow of HOPS-370 (producing arc 2) does not appear to affect the highly collimated jet from VLA15. This indicates that the outflow and the jet are spatially separated, hence the proximity of arc 2 to the VLA15 jet is merely a projection effect. This result, as well as the spatial dichotomy between the material traced in SiO and that traced by the other

molecular tracers, confirms that the outflow from HOPS-370 has a tangential impact on OMC-2 FIR 4 rather than a direct one, as previously suggested by Tobin et al. (2019).

5. Conclusions

We have investigated the internal structures of the protostellar cluster OMC-2 FIR 4 with ALMA observations at 0.04 pc scale and ∼100 au angular resolution. We mapped the emission of eight different molecular tracers: SiO, CH_3OH, $C^{18}O$, CS, CH_3CN, $H^{13}CN$, HC_3N, and CCH, probing high-density gas and shocks. The analysis was mainly focused on SiO and CH_3OH, and our main conclusions are summarised below.

1. A net of intricate filamentary structures was revealed in all the tracers probing extended structures. One of the filamentary structures is aligned with one of the fibres observed in N_2H^+ by Hacar et al. (2018), and the other short filamentary structures could be connected to the intra-hub fibres that are not resolved at parsec scales.
2. From the analysis of CH_3OH kinematics, we showed that each filament moves at a different velocity. The filamentary structures show supersonic motions likely due to protostellar feedback.
3. We observed SiO imprints on some filamentary structures suggesting that they trace compressed and/or shocked gas.
4. SiO emission unveiled multiple bow-shock features with sizes between ∼500 and 2700 au. Their geometry and age suggest that they are likely caused by a precessing jet from HOPS-370 that extends from east to west. Their dynamical ages are <800 yr.
5. We observed a spatial dichotomy between SiO and CH_3OH emission within the protocluster, where SiO dominates the western region and CH_3OH dominates the eastern region, suggesting that the jet from HOPS-370 does not directly impact OMC-2 FIR 4.
6. We detected a highly collimated (∼1°) SiO jet extending along the S-N direction with a projected length of ∼5200 au from the embedded protostar VLA15.

In a nutshell, the observations at high-angular resolutions and sub-parsec scales have allowed us to reveal the previously unresolved hub filamentary structures within OMC-2 FIR 4. Our study complements the studies performed at ∼1 pc scales using N_2H^+, and indicates that the formation of such complex structures could show how cluster-forming regions evolve, with the material being compressed within narrow filaments due to protostellar feedback. Imaging multiple molecular lines is hence important to characterise the gas properties and the processes at play within OMC-2 FIR 4 and other protoclusters.

Acknowledgements. This project has received funding from the European Union's Horizon 2020 research and innovation program under the Marie Skłodowska-Curie grant agreement no. 811312 for the Project "Astro-Chemical Origin" (ACO). This paper makes use of the following ALMA data: ADS/JAO.ALMA 2016.1.00376.S. ALMA is a partnership of ESO (representing its member states), NSF (USA) and NINS (Japan), together with NRC (Canada), MOST and ASIAA (Taiwan), and KASI (Republic of Korea), in cooperation with the Republic of Chile. The Joint ALMA Observatory is operated by ESO, AUI/NRAO and NAOJ. CCo and LP acknowledges the project PRIN-INAF 2016 The Cradle of Life – GENESIS-SKA (General Conditions in Early Planetary Systems for the rise of life with SKA), and the PRIN-MUR 2020 MUR BEYOND-2p (Astrochemistry beyond the second period elements, Prot. 2020AFB3FX). A.L.S., C.C., C.Co., M.D.S. and M.B. acknowledge the funding from the European Research Council (ERC) under the European Union's Horizon 2020 research and innovation program, for the Project "The Dawn of Organic Chemistry" (DOC), grant agreement no. 741002.

References

Adams, F. C. 2010, ARA&A, 48, 47
André, P., Di Francesco, J., Ward-Thompson, D., et al. 2014, in Protostars and Planets VI, eds. H. Beuther, R. S. Klessen, C. P. Dullemond, & T. Henning, 27
Aso, Y., Tatematsu, K., Sekimoto, Y., et al. 2000, ApJS, 131, 465
Bally, J., Langer, W. D., Stark, A. A., & Wilson, R. W. 1987, ApJ, 312, L45
Bouvier, M., López-Sepulcre, A., Ceccarelli, C., et al. 2020, A&A, 636, A19
Cabrit, S., Codella, C., Gueth, F., et al. 2007, A&A, 468, L29
Caselli, P., Hartquist, T. W., & Havnes, O. 1997, A&A, 322, 296
Ceccarelli, C., Dominik, C., López-Sepulcre, A., et al. 2014, ApJ, 790, L1
Chahine, L., López-Sepulcre, A., Neri, R., et al. 2022, A&A, 657, A78
Chen, X., Ellingsen, S. P., Shen, Z.-Q., Titmarsh, A., & Gan, C.-G. 2011, ApJS, 196, 9
Chen, X., Ellingsen, S. P., Ren, Z.-Y., et al. 2019, ApJ, 877, 90
Chini, R., Reipurth, B., Ward-Thompson, D., et al. 1997, ApJ, 474, L135
Chung, E. J., Lee, C. W., Kim, S., et al. 2021, ApJ, 919, 3
Clark, B. G. 1980, A&A, 89, 377
Codella, C., Cabrit, S., Gueth, F., et al. 2007, A&A, 462, L53
Codella, C., Maury, A. J., Gueth, F., et al. 2014, A&A, 563, A3
Cosentino, G., Jiménez-Serra, I., Caselli, P., et al. 2019, ApJ, 881, L42
Cosentino, G., Jiménez-Serra, I., Henshaw, J. D., et al. 2020, MNRAS, 499, 1666
Crimier, N., Ceccarelli, C., Lefloch, B., & Faure, A. 2009, A&A, 506, 1229
Cuadrado, S., Goicoechea, J. R., Cernicharo, J., et al. 2017, A&A, 603, A124
Dartois, E., Chabot, M., Id Barkach, T., et al. 2019, A&A, 627, A55
De Simone, M., Codella, C., Ceccarelli, C., et al. 2022, MNRAS, 512, 5214
Draine, B. T., Roberge, W. G., & Dalgarno, A. 1983, ApJ, 264, 485
Duley, W. W., & Williams, D. A. 1993, MNRAS, 260, 37
Evans, L., Fontani, F., Vastel, C., et al. 2022, A&A, 657, A136
Favre, C., Ceccarelli, C., López-Sepulcre, A., et al. 2018, ApJ, 859, 136
Feddersen, J. R., Arce, H. G., Kong, S., et al. 2018, ApJ, 862, 121
Flower, D. R., & Pineau des Forets, G. 1994, MNRAS, 268, 724
Fontani, F., Ceccarelli, C., Favre, C., et al. 2017, A&A, 605, A57
Fontani, F., Quaia, G., Ceccarelli, C., et al. 2020, MNRAS, 493, 3412
Furlan, E., Megeath, S. T., Osorio, M., et al. 2014, ApJ, 786, 26
Goldsmith, P. F., Heyer, M., Narayanan, G., et al. 2008, ApJ, 680, 428
González-García, B., Manoj, P., Watson, D. M., et al. 2016, A&A, 596, A26
Gounelle, M., Chaussidon, M., & Rollion-Bard, C. 2013, ApJ, 763, L33
Gratier, P., Bron, E., Gerin, M., et al. 2017, A&A, 599, A100
Grossschedl, J. E., Alves, J., Meingast, S., et al. 2018, VizieR Online Data Catalog: J/A+A/619/A106
Guillet, V., Pineau Des Forêts, G., & Jones, A. P. 2011, A&A, 527, A123
Gusdorf, A., Cabrit, S., Flower, D. R., & Pineau Des Forêts, G. 2008a, A&A, 482, 809
Gusdorf, A., Pineau Des Forêts, G., Cabrit, S., & Flower, D. R. 2008b, A&A, 490, 695
Hacar, A., & Tafalla, M. 2011, A&A, 533, A34
Hacar, A., Tafalla, M., Kauffmann, J., & Kovács, A. 2013, A&A, 554, A55
Hacar, A., Alves, J., Tafalla, M., & Goicoechea, J. R. 2017a, A&A, 602, A2
Hacar, A., Tafalla, M., & Alves, J. 2017b, A&A, 606, A123
Hacar, A., Tafalla, M., Forbrich, J., et al. 2018, A&A, 610, A77
Hacar, A., Clark, S., Heitsch, F., et al. 2022, ApJ, submitted [arXiv:2203.09562]
Henshaw, J. D., Caselli, P., Fontani, F., et al. 2013, MNRAS, 428, 3425
Henshaw, J. D., Caselli, P., Fontani, F., Jiménez-Serra, I., & Tan, J. C. 2014, MNRAS, 440, 2860
Henshaw, J. D., Jiménez-Serra, I., Longmore, S. N., et al. 2017, MNRAS, 464, L31
Hunter, T. R., Brogan, C. L., Cyganowski, C. J., & Young, K. H. 2014, ApJ, 788, 187
Jiménez-Serra, I., Caselli, P., Tan, J. C., et al. 2010, MNRAS, 406, 187
Johnstone, D., & Bally, J. 1999, ApJ, 510, L49
Johnstone, D., Boonman, A. M. S., & van Dishoeck, E. F. 2003, A&A, 412, 157
Kainulainen, J., Stutz, A. M., Stanke, T., et al. 2017, A&A, 600, A141
Kama, M., López-Sepulcre, A., Dominik, C., et al. 2013, A&A, 556, A57
Kama, M., Caux, E., López-Sepulcre, A., et al. 2015, A&A, 574, A107
Kang, M., Lee, J.-E., Choi, M., et al. 2013, ApJS, 209, 25
Kogan, L., & Slysh, V. 1998, ApJ, 497, 800
Ladeyschikov, D. A., Urquhart, J. S., Sobolev, A. M., Breen, S. L., & Bayandina, O. S. 2020, AJ, 160, 213
Lattanzi, V., Alves, F., Padovani, M., et al. 2021, A&A, submitted
Lee, C.-F., Hirano, N., Zhang, Q., et al. 2015, ApJ, 805, 186
Lee, C.-F., Ho, P. T. P., Li, Z.-Y., et al. 2017, Nat. Astron., 1, 0152
Leurini, S., Schilke, P., Menten, K. M., et al. 2004, A&A, 422, 573
Leurini, S., Parise, B., Schilke, P., Pety, J., & Rolffs, R. 2010, A&A, 511, A82
Li, D., Kauffmann, J., Zhang, Q., & Chen, W. 2013, ApJ, 768, L5

López-Sepulcre, A., Kama, M., Ceccarelli, C., et al. 2013a, A&A, 549, A114
López-Sepulcre, A., Taquet, V., Sánchez-Monge, Á., et al. 2013b, A&A, 556, A62
López-Sepulcre, A., Watanabe, Y., Sakai, N., et al. 2016, ApJ, 822, 85
López-Sepulcre, A., Sakai, N., Neri, R., et al. 2017, A&A, 606, A121
Manoj, P., Watson, D. M., Neufeld, D. A., et al. 2013, ApJ, 763, 83
Maret, S., Ceccarelli, C., Tielens, A. G. G. M., et al. 2005, A&A, 442, 527
Martin-Pintado, J., Rodriguez-Franco, A., & Bachiller, R. 1990, ApJ, 357, L49
McMullin, J. P., Waters, B., Schiebel, D., Young, W., & Golap, K. 2007, in Astronomical Society of the Pacific Conference Series, Astronomical Data Analysis Software and Systems XVI, eds. R. A. Shaw, F. Hill, & D. J. Bell, 376, 127
Mezger, P. G., Wink, J. E., & Zylka, R. 1990, A&A, 228, 95
Minissale, M., Dulieu, F., Cazaux, S., & Hocuk, S. 2016, A&A, 585, A24
Molinari, S., Bally, J., Glover, S., et al. 2014, in Protostars and Planets VI, eds. H. Beuther, R. S. Klessen, C. P. Dullemond, & T. Henning, 125
Müller, H. S. P., Thorwirth, S., Roth, D. A., & Winnewisser, G. 2001, A&A, 370, L49
Müller, H. S. P., Schlöder, F., Stutzki, J., & Winnewisser, G. 2005, J. Mol. Struct., 742, 215
Myers, P. C. 1983, ApJ, 270, 105
Myers, P. C. 2009, ApJ, 700, 1609
Nesterenok, A. V. 2022, MNRAS, 509, 4555
Orkisz, J. H., Peretto, N., Pety, J., et al. 2019, A&A, 624, A113
Osorio, M., Díaz-Rodríguez, A. K., Anglada, G., et al. 2017, ApJ, 840, 36
Pfalzner, S., Davies, M. B., Gounelle, M., et al. 2015, Phys. Scr, 90, 068001
Pihlström, Y. M., Sjouwerman, L. O., Frail, D. A., et al. 2014, AJ, 147, 73
Podio, L., Tabone, B., Codella, C., et al. 2021, A&A, 648, A45
Polychroni, D., Schisano, E., Elia, D., et al. 2013, ApJ, 777, L33
Ray, T. P., & Ferreira, J. 2021, New A Rev., 93, 101615
Rimola, A., Taquet, V., Ugliengo, P., Balucani, N., & Ceccarelli, C. 2014, A&A, 572, A70
Rodriguez-Franco, A., Martin-Pintado, J., Gomez-Gonzalez, J., & Planesas, P. 1992, A&A, 264, 592
Schilke, P., Walmsley, C. M., Pineau des Forets, G., & Flower, D. R. 1997, A&A, 321, 293
Schöier, F. L., van der Tak, F. F. S., van Dishoeck, E. F., & Black, J. H. 2005, A&A, 432, 369
Shimajiri, Y., Takahashi, S., Takakuwa, S., Saito, M., & Kawabe, R. 2008, ApJ, 683, 255
Shimajiri, Y., Kawabe, R., Takakuwa, S., et al. 2011, PASJ, 63, 105
Shimajiri, Y., Sakai, T., Kitamura, Y., et al. 2015, ApJS, 221, 31
Shirley, Y. L. 2015, PASP, 127, 299
Sobolev, A. M., Cragg, D. M., Ellingsen, S. P., et al. 2007, in Astrophysical Masers and their Environments, eds. J. M. Chapman, & W. A. Baan, 242, 81
Sokolov, V., Wang, K., Pineda, J. E., et al. 2019, ApJ, 872, 30
Suri, S., Sánchez-Monge, Á., Schilke, P., et al. 2019, A&A, 623, A142
Tafalla, M., & Hacar, A. 2015, A&A, 574, A104
Takahashi, S., Saito, M., Ohashi, N., et al. 2008, ApJ, 688, 344
Tatematsu, K., Kandori, R., Umemoto, T., & Sekimoto, Y. 2008, PASJ, 60, 407
Tielens, A. G. G. M., & Hagen, W. 1982, A&A, 114, 245
Tobin, J. J., Megeath, S. T., van't Hoff, M., et al. 2019, ApJ, 886, 6
Voronkov, M. A., Brooks, K. J., Sobolev, A. M., et al. 2006, MNRAS, 373, 411
Voronkov, M. A., Caswell, J. L., Ellingsen, S. P., & Sobolev, A. M. 2010, MNRAS, 405, 2471
Voronkov, M. A., Caswell, J. L., Ellingsen, S. P., Green, J. A., & Breen, S. L. 2014, MNRAS, 439, 2584
Watanabe, N., & Kouchi, A. 2002, ApJ, 571, L173
Williams, J. P., Plambeck, R. L., & Heyer, M. H. 2003, ApJ, 591, 1025
Wu, Y., Zhang, Q., Chen, H., et al. 2005, AJ, 129, 330
Wu, G., Qiu, K., Esimbek, J., et al. 2018, A&A, 616, A111
Zhang, C., Ren, Z., Wu, J., et al. 2020, MNRAS, 497, 793

Appendix A: Spectra

We report in Fig. A.1 the spectra of CH_3OH ($4_{-2,3}-3_{-1,2}$ E) masers, observed at three spots along the eastern ridge of OMC-2 FIR 4. In Fig. A.2 we show the CH_3OH ($5_{1,4}-4_{1,3}$ A) spectra extracted from the different positions shown Fig. 4. In Fig. A.3 we present an SiO spectrum extracted at a position along the eastern ridge.

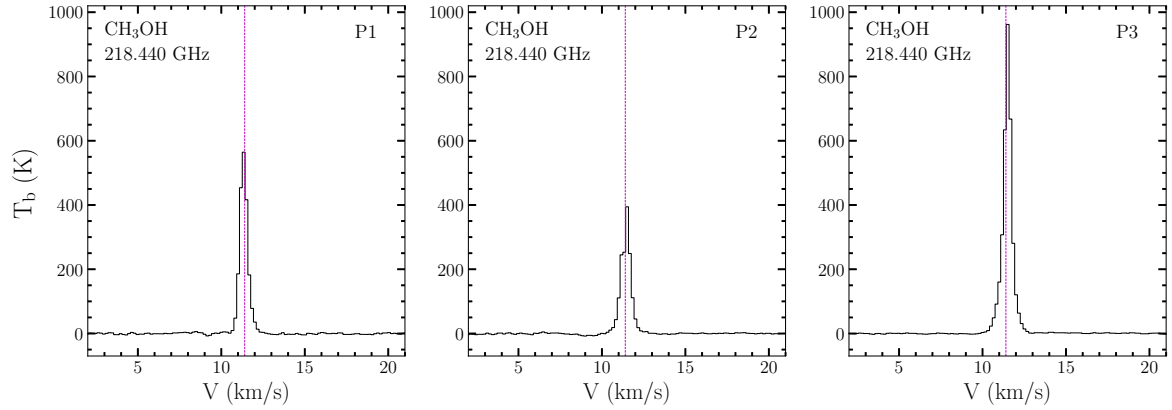

Fig. A.1. Spectra of the masers detected in $CH_3OH(4_{-2,3}-3_{-1,2}$ E) at the P1-P3 positions. The vertical dashed line stands for the systemic velocity of OMC-2 FIR 4

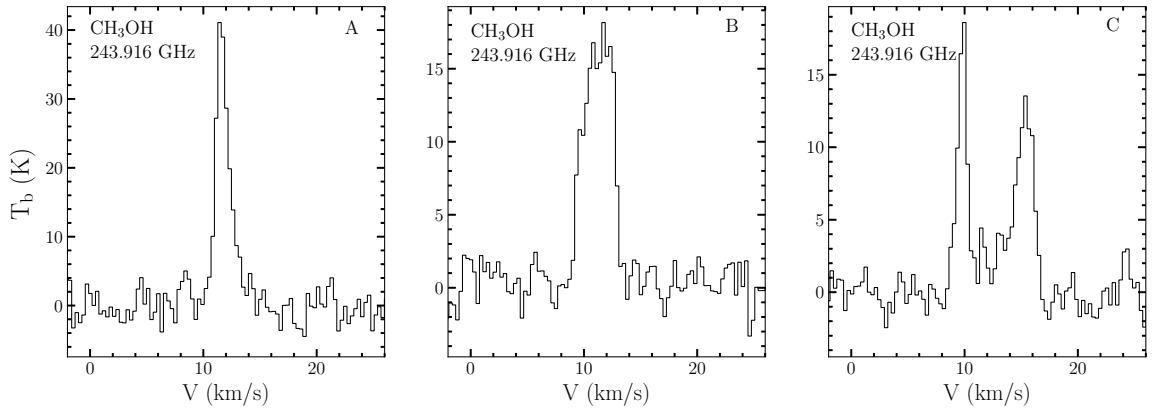

Fig. A.2. CH_3OH ($5_{1,4}-4_{1,3}$ A) spectra extracted from three different positions (A, B, and C) shown in the moment-2 map (See Fig. 4). The first shows a region with low-velocity dispersion, the second shows a region with intermediate-velocity dispersion, and the third shows the central region with several components along the line of sight.

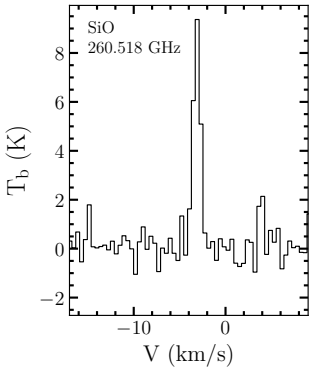

Fig. A.3. SiO emission representative of the eastern ridge extracted at the position (6.5″,2.1″)

Appendix B: Jet simulation

In this section, we describe the simulation that we have performed to verify that the narrow opening angle of the jet is not the result of interferometric filtering. We first created rectangular structures with a fixed length and different widths between 1/6 and 10 times the size of the synthesised beam (~0.″05–3.″2). The interferometric response to each structure was determined by entering the visibilities corresponding to each structure into the SiO jet uv-table. The visibility weights were kept unchanged. To investigate the influence of thermal noise on the image reconstruction, Gaussian noise was added to the visibilities according to their weights. Finally, the uv-table of each structure was Fourier-transformed to produce a dirty map, and was then cleaned. The results are shown for a possible thermal noise model in Fig. B.1.

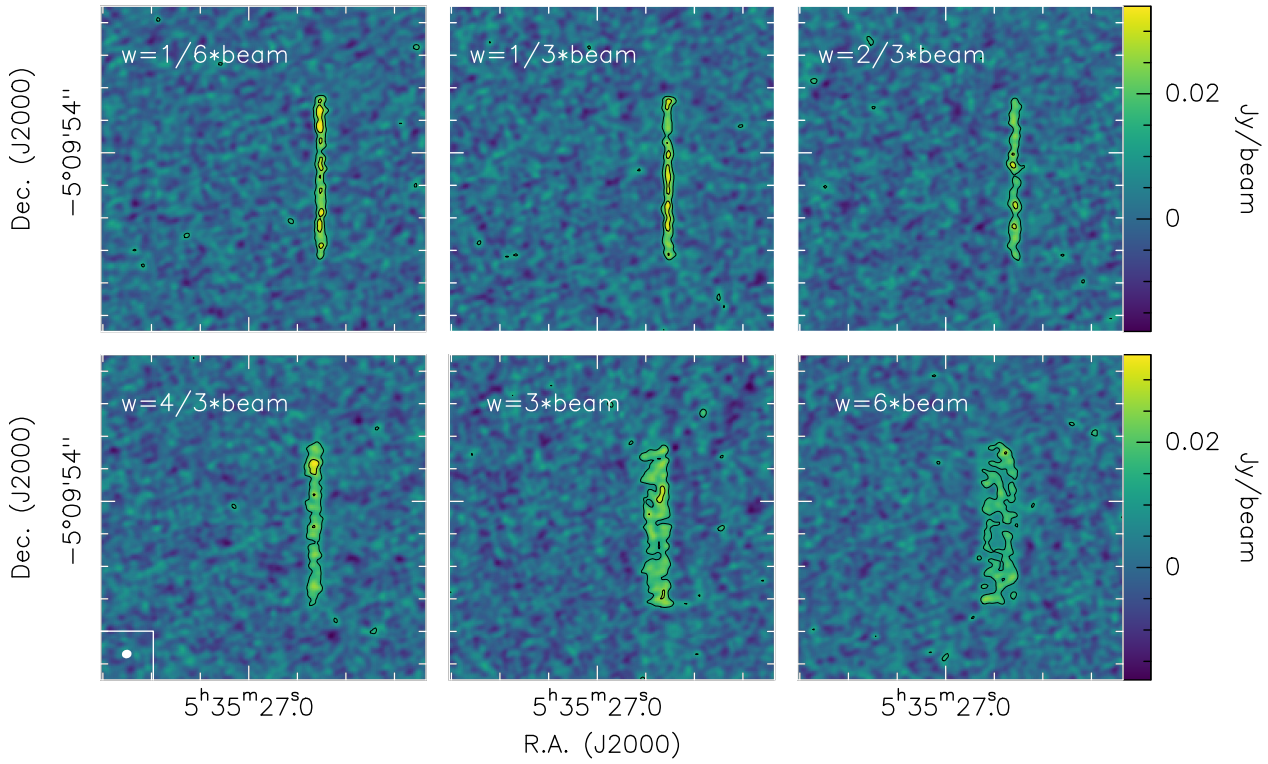

Fig. B.1. Interferometric response to each structure after running the model. The width w of the rectangular (jet-like) structures given as input in the model is depicted in white in the upper left corner. The synthesised beam is depicted in white in the lower left corner. The colour scale is the same for all the panels. The box size is 5”×5”.

Appendix C: Maps

In Fig. C.1 we present the dust emission with superimposed contours of the velocity-integrated emission of SiO at different velocity regimes discussed in the main text. In Figs. C.2-C.6 we report the channels maps of $CH_3OH(5_{1,4}-4_{1,3}$ A), $CH_3OH(4_{-2,3}-3_{-1,2}$ E), HC_3N(3–2), $C^{18}O$(2–1), $CH_3OH(4_{2,3}-5_{1,4}$ E), CS(5–4), and SiO(6–5).

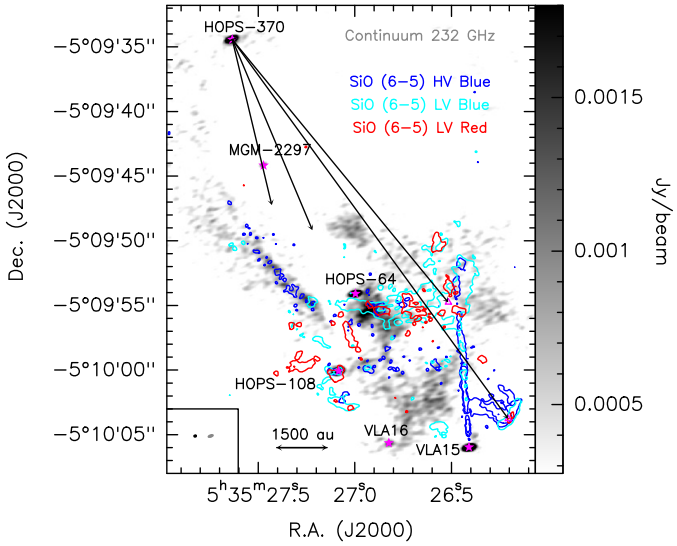

Fig. C.1. Continuum emission at 232 GHz in colours, with superimposed contours of the velocity-integrated emission of SiO at different velocity regimes. The colour images are for intensities higher than 3σ with $\sigma = 91.7$ μJy beam^{-1}. The SiO contours are at 5σ with $\sigma = 5.8$ mJy beam^{-1} km s^{-1}. They correspond to the blueshifted high-velocity regime (blue), the blueshifted low-velocity regime (cyan), and the redshifted low-velocity regime (red) (See Sect. 3.2). The different cores are depicted with magenta stars and are labelled in black. The positions of the SiO peaks from this study are depicted with open magenta triangles. We draw four arrows from HOPS-370, one perpendicular to the disk, two towards the SiO peaks, and one similar to the direction of the jet in [O I] by González-García et al. (2016). The synthesised beam of SiO and continuum are depicted in the lower left corner in blue and grey, respectively.

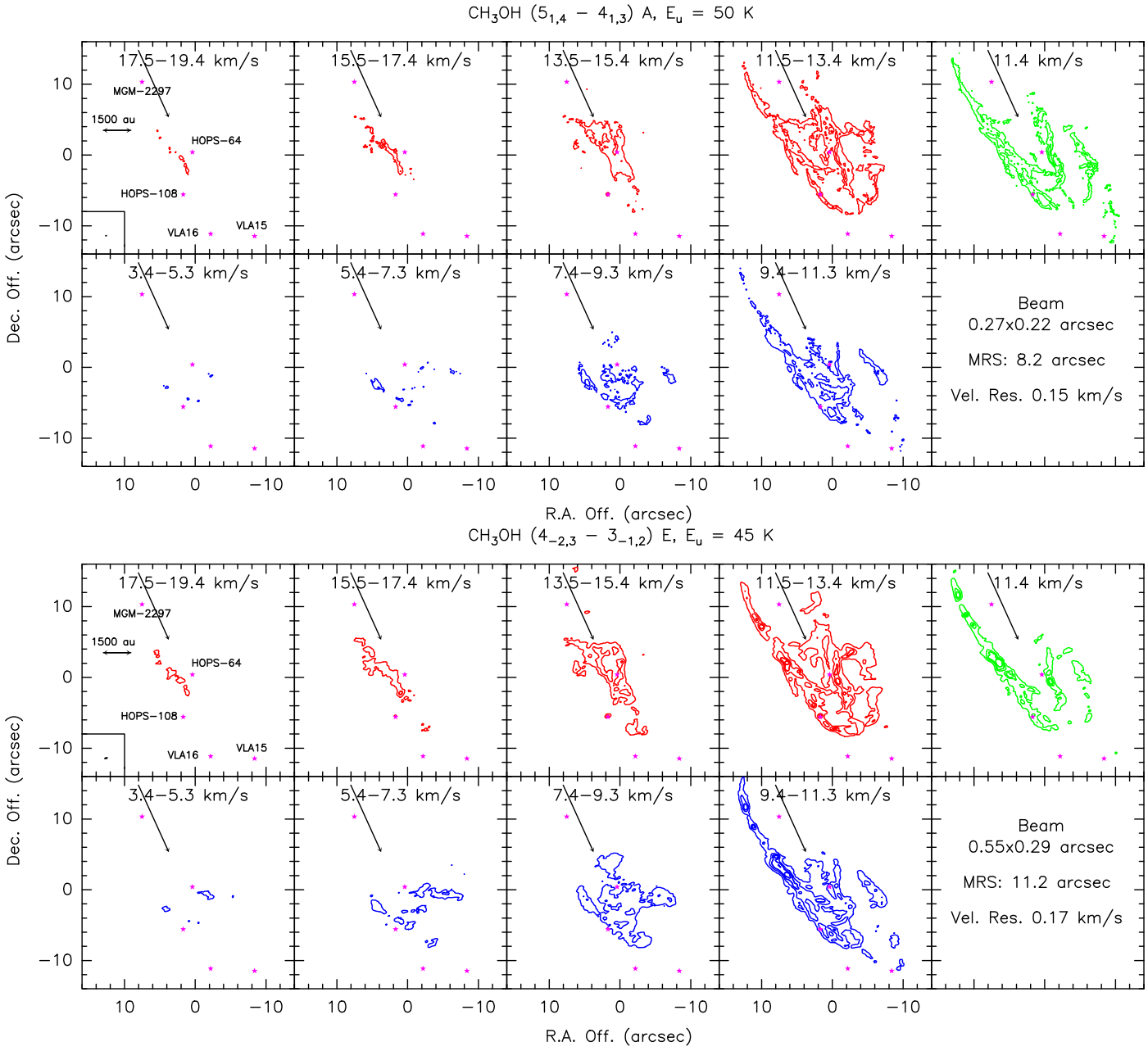

Fig. C.2. Channel maps of methanol at 50 K (top) and 45 K (bottom). The contours are at [5,20]σ (top) and [5, 20, 40, 80]σ (bottom) with σ= (5 mJy beam^{-1} km s^{-1} top, and 8 mJy beam^{-1} km s^{-1} bottom). The cores are depicted with magenta stars and are labelled in black. The synthesised beam is depicted in the lower left corner. We draw one arrow from HOPS-370 perpendicular to its disk. The beam, maximum recoverable angular scale (MRS), and velocity resolution values are reported in the bottom right panel.

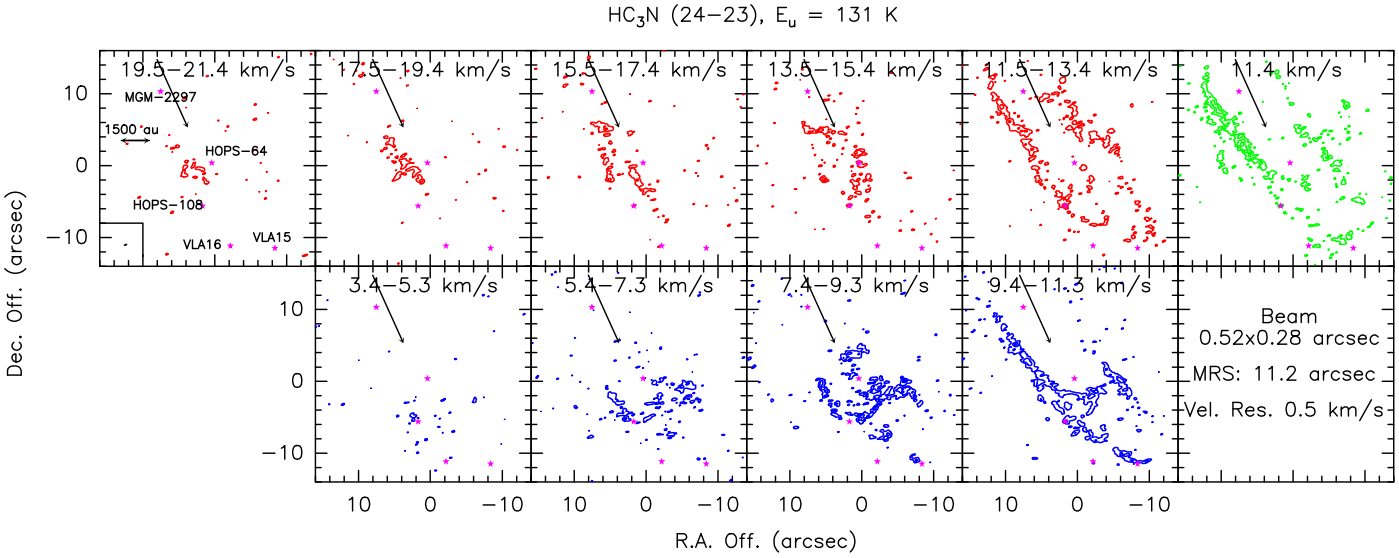

Fig. C.3. Channel maps of HC_3N. Contours start at 3σ and increase by 5σ with σ= 4 mJy beam^{-1} km s^{-1}. The cores are depicted with magenta stars and are labelled in black. The synthesised beam is depicted in the lower left corner. We draw one arrow from HOPS-370 perpendicular to its disk. The beam, MRS, and velocity resolution values are reported in the bottom right panel.

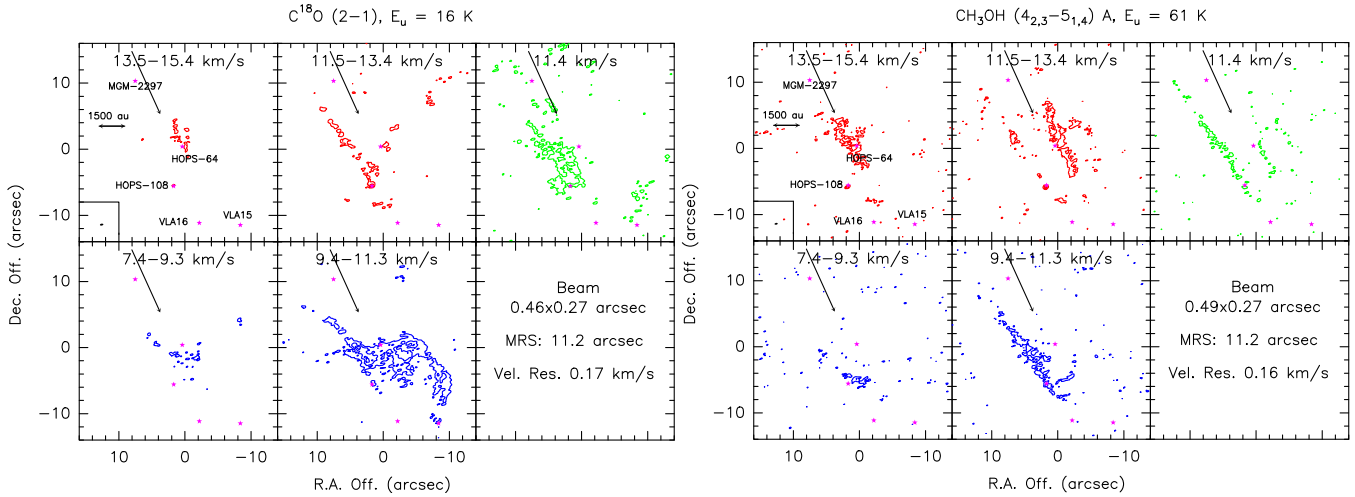

Fig. C.4. Channel maps of C^{18}O (left) and CH_3OH at 61 K (right). Contours start at 5σ for C^{18}O, and 3σ for CH_3OH and increase by 5σ with σ= (4 mJy beam^{-1} km s^{-1} left, and 6 mJy beam^{-1} km s^{-1} right). The cores are depicted with magenta stars and are labelled in black. The synthesised beam is depicted in the lower left corner. We draw one arrow from HOPS-370 perpendicular to its disk. The beam, MRS, and velocity resolution values are reported in the bottom right panel.

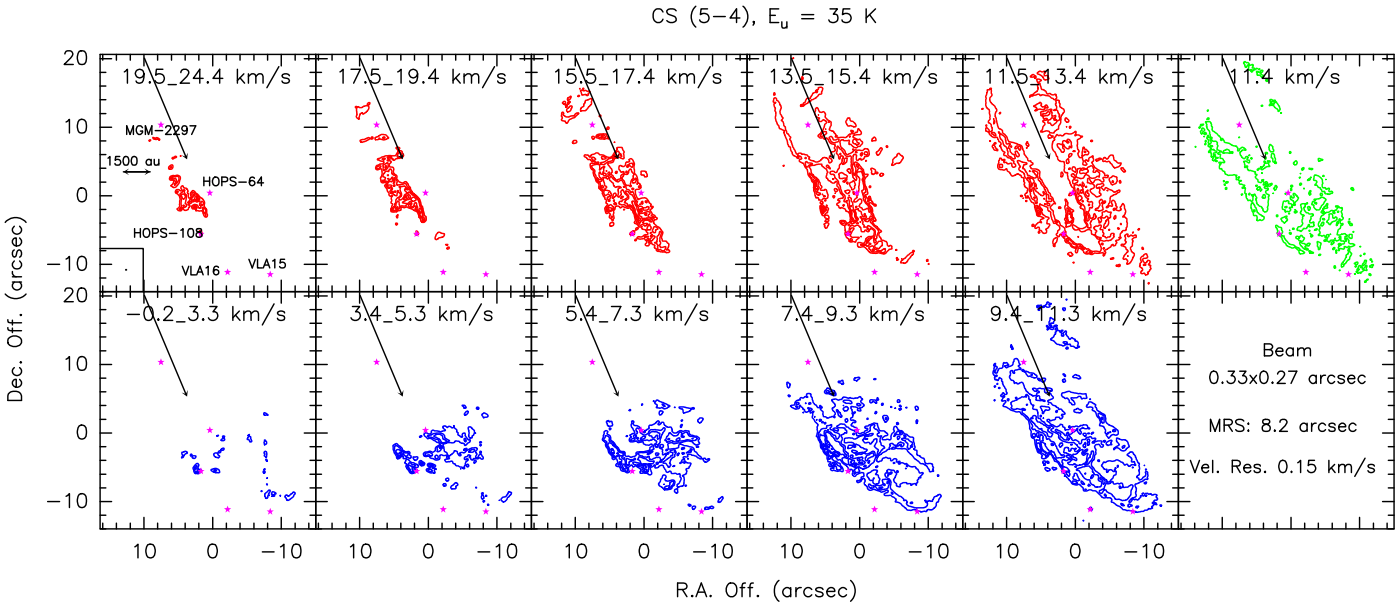

Fig. C.5. Channel maps of CS. The contours are at [5, 20, 40]σ with σ= 4 mJy beam^{-1} km s^{-1}. The cores are depicted with magenta stars and are labelled in black. The synthesised beam is depicted in the lower left corner. We draw one arrow from HOPS-370 perpendicular to its disk. The beam, MRS, and velocity resolution values are reported in the bottom right panel.

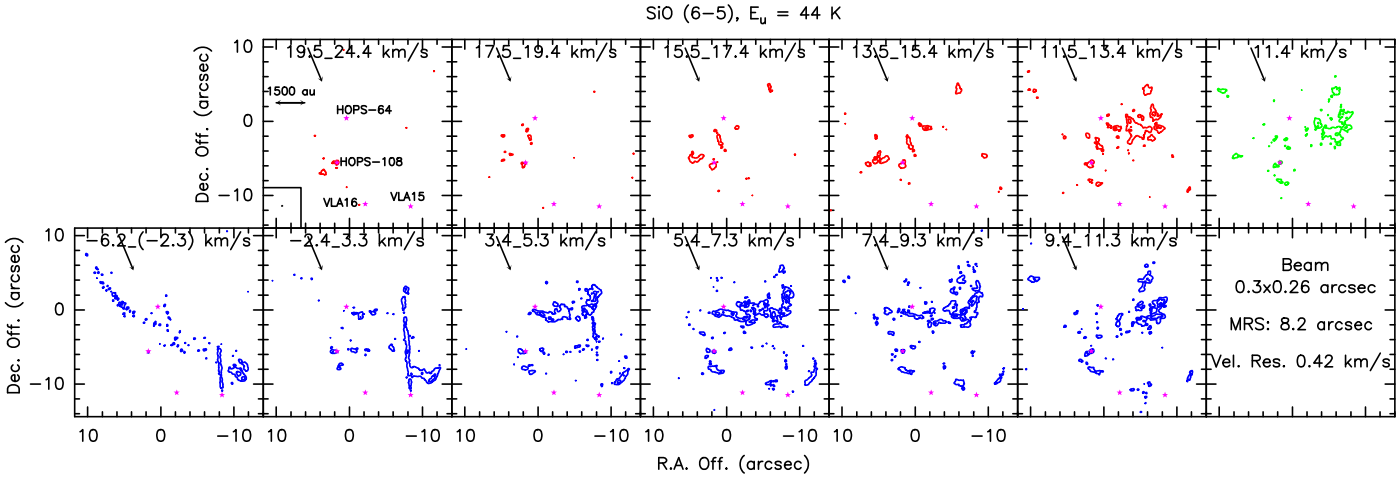

Fig. C.6. Channel maps of SiO. The contours are at [5, 20, 40]σ with σ= 2.5 mJy beam^{-1} km s^{-1}. The cores are depicted with magenta stars and are labelled in black. The synthesised beam is depicted in the lower left corner. We draw one arrow from HOPS-370 perpendicular to its disk. The beam, MRS, and velocity resolution values are reported in the bottom right panel.